

Transitional cylindrical swirling flow in presence of a flat free surface

Roland Bouffanais ^{a,b,*,1}, David Lo Jacono ^c

^a*Laboratory of Computational Engineering,
École Polytechnique Fédérale de Lausanne,
STI-IGM-LIN, Station 9,
CH-1015 Lausanne, Switzerland*

^b*Present address: Massachusetts Institute of Technology,
Department of Mechanical Engineering,
77 Massachusetts Avenue, Bldg 5-326,
Cambridge, MA 02139*

^c*Department of Mechanical and Aerospace Engineering,
Monash University,
Victoria, 3800 Melbourne, Australia*

Abstract

This article is devoted to the study of an incompressible viscous flow of a fluid partly enclosed in a cylindrical container with an open top surface and driven by the constant rotation of the bottom wall. Such type of flows belongs to a group of recirculating lid-driven cavity flows with geometrical axisymmetry and of the prescribed boundary conditions of Dirichlet type—no-slip on the cavity walls. The top surface of the cylindrical cavity is left open with an imposed stress-free boundary condition, while a no-slip condition with a prescribed rotational velocity is imposed on the bottom wall. The Reynolds regime corresponds to transitional flows with some incursions in the fully laminar regime. The approach taken here revealed new flow states that were investigated based on a fully three-dimensional solution of the Navier–Stokes equations for the free-surface cylindrical swirling flow, without resorting to any symmetry property unlike all other results available in the literature. These solutions are obtained through direct numerical simulations based on a Legendre spectral element method.

Key words: Swirling flow, free surface, vortex breakdown, lid-driven cavity

* Corresponding author.

Email addresses: bouffana@mit.edu (Roland Bouffanais), david.lojacono@eng.monash.edu.au (David Lo Jacono).

¹ Supported by a Swiss National Science Foundation Grant No. 200020–101707

1 Introduction

Besides the differences in terms of geometry, the lid-driven cubical cavity flow [1] and the cylindrical swirling flow investigated in this article, present similar features typical of shear-driven recirculating flows such as intense wall-jets, shear layers in the vicinity of the driven wall, and secondary recirculating flows, all of which are very dependent on the flow parameters. Nevertheless, the geometry—cubical on one hand and cylindrical on the other hand—dramatically influences the nature and structure of these secondary flows: corner eddies for the cubical cavity and recirculation bubbles or vortex breakdown in the cylindrical case.

1.1 General considerations

Following the pioneering work of Bogatyrev & Gorin [2] and Koseff & Street [3, 4], it was shown that contrary to intuition, the lid-driven *cubical* cavity flow is essentially three-dimensional, even when considering large aspect ratio. It is only recently that the three-dimensionality of the lid-driven *cylindrical* cavity flow was confirmed numerically by Blackburn & Lopez [5, 6] after it was suggested but not fully proved experimentally by Sørensen [7], Spohn et al. [8], Sotiropoulos & Ventikos [9], and Pereira & Sousa [10]. In 2001, Sotiropoulos & Ventikos [11] gave full experimental evidence of the three-dimensional character of the flow with the onset of non-axisymmetric modes. The three-dimensional nature of these driven cavity flows therefore appears as a general characteristic of internal recirculating shear-driven flows.

In the sequel, we will only consider the cylindrical lid-driven cavity flow also referred to as “swirling” flow without any additional precision. The first experiments by Vogel [12] and later Ronnenberg [13] showed that Ekman suction and pumping, induced by the Ekman layers on the rotating and stationary disks, lead to the formation of a concentrated vortex core along the axis in the closed cavity case. The two dimensionless numbers characterizing this flow are the height-to-radius aspect ratio $\Lambda = H/R$ and the Reynolds number $Re = R^2\Omega/\nu$, where H and R are the height and radius of the cylinder respectively, Ω the constant angular velocity of the bottom end-wall, and ν the kinematic viscosity of the Newtonian fluid. For specific values of the aspect ratio Λ , and above a critical Reynolds number, the vortex core breaks down in the form of one or more recirculation bubbles which are on-axis in the closed cavity case and on- or off-axis in the open cavity case. Owing to the enormous extent of work in the area of vortex breakdown (VB), (see reviews by Hall [14], Leibovich [15], Shtern & Hussain [16], Kerswell [17], and Arndt [18]), we will only briefly recall the central features of VB. As defined by Leibovich in its review on the structure of vortex breakdown [15], the term “vortex breakdown” refers to a disturbance characterized by the formation of an internal stagnation point on the vortex axis, followed by reversed flow in a region of limited axial extent. Two forms of vortex breakdown predominate, one called “near-axisymmetric” (sometimes “axisymmetric” or “bubble-like”), and the other called “spiral”.

The practical importance of vortex breakdown lies mainly in the field of aeronautics, where they can be observed over wings—mainly delta wings—with highly swept leading edges when the angle of incidence exceeds a critical value. Vortex breakdown can be a limiting factor on the operating altitude of slender-winged flying vehicles. Moreover, the occurrence of VB in the wake of a large

aircraft is relevant to the safety of flight in dense air-traffic, which is becoming more and more frequent with the constant increase in air-traffic over the years. VB is also important in other fields for example it has been observed in the swirling flows through nozzles and diffusers [19], and in the field of reactive flows, in combustion chambers. Besides the tremendous importance of VB in engineering applications, it is also a prototypical phenomenon allowing to elucidate the fundamental aspects of the bubble mode.

1.2 The lid-driven cylindrical cavity flow

The first comprehensive experimental study of the closed cylindrical container case was undertaken by Escudier [20], and Escudier & Keller [21], who extended the earlier results of Vogel [12] and Ronnenberg [13] to obtain the first map of VB transitions with respect to the aspect ratio Λ and the Reynolds number. Escudier [20] revealed flow states with one, two or even three successive breakdowns, as well as a transition from steadiness to unsteadiness. Sørensen [7] extended to a broader range of Reynolds number in the same experiment as Escudier [20] for the closed container, and inferred that above a critical Reynolds number in the unsteady flow regime, the meridional flow becomes highly asymmetric. The first experimental study of the open cylindrical container case with a free surface on the top, was undertaken by Spohn et al. [22], who highlighted the significant change in the structure, the occurrence and the location of the breakdown bubbles. In the steady closed cylinder case, Hourigan et al. [23] investigated the asymmetric spiraling effects along the cylinder axis prior to the first vortex breakdown. They argued that the observed asymmetry was purely an experimental artifact and not an evidence of the three-dimensional nature of the flow. Spohn et al. [8] were the first to investigate experimentally the origin of possible asymmetric features of the instabilities at their onset. The steady breakdown bubbles reported by Spohn et al. [8] showcase asymmetric features comparable to earlier measurements, and also to unsteady bubbles observed in circular diffusers by Faler & Leibovich [19]. As a matter of fact, the work of Spohn et al. [8] is really a pioneering work in the acceptance of the axisymmetry breaking, amongst fluid experimentalists, see Brøns et al. [24]. It is noteworthy at this point, that the complex physics associated with these intricate phenomena occurring in closed/open rotating cylindrical container is still not clearly understood.

Like for the lid-driven cubical cavity flow, and in relation with the simple geometry of the flow, the rotating cylindrical cavity flow has been extensively studied using direct numerical simulations. It is important to note that since the early seventies, the method of choice has consisted in solving the streamfunction-vorticity formulation of the axisymmetric incompressible Navier–Stokes equations. Without being exhaustive, the following list of references gives an overview of the numerical simulation of the closed lid-driven cylindrical flow over three decades: Pao [25], Lugt & Haussling [26, 27], Dijkstra & van Heijst [28], Lugt & Abboud [29], Neitzel [30], Daube & Sørensen [31], Lopez [32], Brown & Lopez [33], Lopez & Perry [34], Sørensen & Christensen [35], Watson & Neitzel [36], Gelfgat et al. [37, 38], Tsitverblit & Kit [39], and Brøns et al. [40]. All these works were able to reproduce with a reasonable accuracy, the basic features observed experimentally and reported earlier including the size, shape and number of recirculation bubbles. The onset of vortex breakdown was to some extent captured by several of these numerical simulations. Lopez [32], and Brown & Lopez [33] suggested a physical mechanism for the intricate phenomena observed. They prove the existence of a standing centrifugal wave, whose amplitude increases with the Reynolds number and which can create a stagnation point on

the cylinder axis, initiating the breakdown process. It is worth recalling that the streamfunction-vorticity formulation is adequate and appropriate only for the study of flow dynamics preserving the property of axisymmetry. At the inception of any instability breaking the axisymmetry of the flow, a three-dimensional solution of the Navier–Stokes equations is required, thereby increasing considerably the complexity of the task. The last remark justifies the observed changes in terms of numerical modeling of Lopez’ group and Sørensen’s group, to allow them to investigate axisymmetry breaking in the closed cylinder case [5,6,41–43]. Therefore, three-dimensional flow structures have started being simulated more recently, see Gelfgat et al. [44], Sotiropoulos & Ventikos [11], Sotiropoulos et al. [45], Marques & Lopez [46], Blackburn & Lopez [5,6], Serre & Bontoux [47], Blackburn [48], and Lopez [49].

Apart from the canonical case with a single driving lid in rotation at a constant angular velocity, different variations of the problem have been extensively studied in the past years: e.g. cylinder with co- and counter-rotating end-covers by Brøns et al. [40], steady axisymmetric flow in an open cylindrical container with a partially rotating bottom wall by Piva & Meiburg [50], vortex scenario and bubble generation in a cylindrical cavity with rotating top and bottom by Okulov et al. [51]. Mullin et al. [52] also included a rod at the axis to control the breakdown, and Pereira & Sousa [10] significantly changed the configuration by replacing the flat rotating bottom cover by a cone. As noted by Brøns et al. [53], all these studies show a large set of flow structures which are quite sensitive to variations of external parameters. Mununga et al. [54] and Lo Jacono et al. [55] investigated different strategies for the control of vortex breakdown.

1.3 *Open swirling flow*

The focus in the present article is on the canonical problem of a cylinder with a rotating bottom end-wall but replacing the stationary solid top end-wall by a free surface. The flow associated with this problem was first studied experimentally by Spohn et al. [8,22]. They observed the influence of the top free surface—assuredly clean of surfactants—on the onset, structure, nature and number of recirculating bubbles. Their central observations are that breakdown bubbles still appear, but are off-axis and may be attached to the free surface, depending on the aspect ratio Λ and the Reynolds number. Of course, such structures could not be observed in the closed case because of the no-slip condition imposed on the top wall. All the past simulations of free-surface swirling flows rely on the central assumptions that the free surface is flat and clean, which means that the Froude number is very small and that surface tension effects are negligible. With these assumptions, the flow is identical to the flow in the lower half part of a cylinder with two solid covers in co-rotation, i.e. rotating at the same angular velocity. Brøns et al. reported a wide range of topologies of vortex breakdown bubbles in a bottom-driven cylinder with a free surface. Valentine & Jahnke [56], observed in their simulations the existence of one or two toroidal-like types of recirculation bubble having their stagnation lines attached to the free surface, depending on the value of the Reynolds number. Their study was complemented by the work of Lopez [57] for oscillating unsteady flows. Information relevant to the present problem with a free surface all indicate consistent flow behavior at small aspect ratio i.e., $0.5 \leq \Lambda \leq 1.0$ in that stagnation occurs off-axis and associated secondary flow creates a toroidal recirculation bubble. Steady free-surface flows have been computed by Iwatsu [58,59] providing flow state classifications with new flow patterns not revealed in the previous studies.

1.4 Motivations and objectives

The present study is motivated by several factors. Firstly, compared to the closed cylinder case, only some limited aspects of the open swirling flow have been investigated so far. The study of this intricate problem is relatively new and consequently the body of knowledge in some (Λ, Re) -parameter regions appears fairly limited. Secondly, most of the past studies involving numerical simulations of this free-surface swirling flow, used axisymmetric streamfunction-vorticity formulations: Brøns et al. [53], Iwatsu [58, 59], and Piva & Meiburg [50]. To our knowledge, the only fully three-dimensional numerical simulations is due to Lopez et al. [60], who investigated mainly symmetry breaking issues.

In the present article, new flow states are investigated based on a fully three-dimensional solution of the Navier–Stokes equations without the need to resort to symmetry properties by doubling the computational domain and enforcing co-rotation of both end-walls. To our knowledge, the present study provides the most general available results for this flat-free-surface problem. Both, steady and unsteady flows are considered for different sets of governing parameters (Λ, Re) . A Legendre spectral element method is used to provide an accurate solution of the governing equations, while the stress-free boundary condition is naturally enforced into the weak formulation of the problem.

The mathematical model and the problem formulation are detailed in Sec. 2, while the original computational approach of this study is presented in Sec. 3. Subsequently, Sec. 4 contains all the numerical results corresponding to various physical situations and flow states. Finally, the article ends with Sec. 5 providing summary and conclusions on the present work.

2 Mathematical model and problem formulation

2.1 Mathematical description of the problem

The fluid enclosed in the cylindrical cavity is assumed to be incompressible, Newtonian with uniform density and temperature. The flow is governed by the Navier–Stokes equations

$$\frac{\partial u_i}{\partial t} + u_j \frac{\partial u_i}{\partial x_j} = \frac{\partial \sigma_{ij}^*}{\partial x_j} + g_i, \quad (1)$$

$$\frac{\partial u_j}{\partial x_j} = 0, \quad (2)$$

where $\sigma_{ij}^* = -p\delta_{ij} + 2\nu D_{ij}$ is the reduced Cauchy stress tensor of the fluid, p the static or reduced pressure, D_{ij} the rate-of-deformation tensor, ν the assuredly constant and uniform kinematic viscosity, and g_i the components of the acceleration of gravity ($g_1 = g_2 = 0$ and $g_3 = -g$). Inside the fluid domain denoted by \mathcal{V} , no-slip boundary conditions are imposed on all cavity walls: the tubular side-wall, the bottom end-wall in steady rotation, see Fig. 1. The mathematical

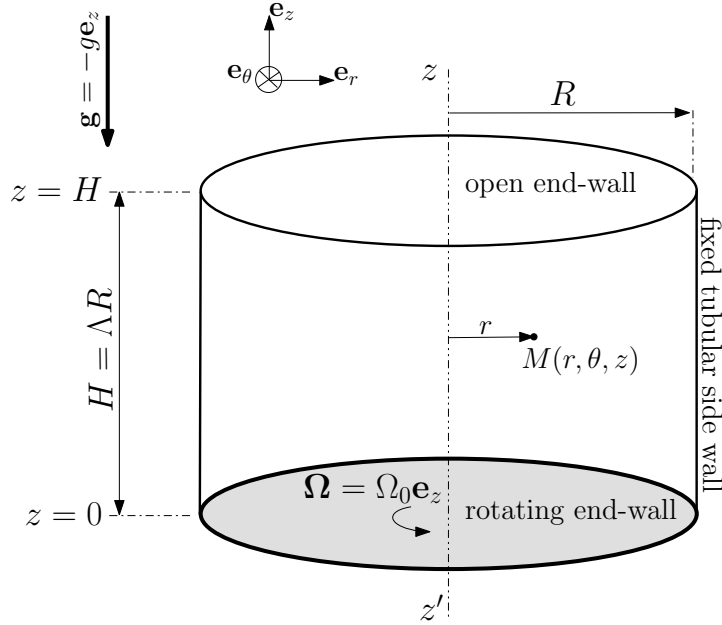


Fig. 1. Schematic of the geometry studied with the set of coordinates employed.

expression of the no-slip condition on the tubular side-wall simply reads

$$u(r = R, \theta, z, t) = v(r = R, \theta, z, t) = w(r = R, \theta, z, t) = 0, \quad 0 \leq \theta \leq 2\pi, \quad 0 \leq z \leq H. \quad (3)$$

The flow is driven by imposing a prescribed angular velocity distribution of the bottom end-wall, which transfers its kinetic energy to the fluid above. The details regarding the imposition of this Dirichlet boundary condition for the velocity field at the lid are discussed in the next section 2.2. The top surface is left open and is modeled as a flat, fixed and clean free surface. The details regarding the imposition of this stress-free condition on the free surface are discussed in Sec. 2.3. As mentioned in the Introduction, Sec. 1.1, two parameters that determine completely the flow state are the height-to-radius aspect ratio $\Lambda = H/R$ and the Reynolds number $\text{Re} = R^2\Omega_0/\nu$, based on the maximal prescribed angular velocity Ω_0 of the bottom end-wall.

In the sequel, the length, time, velocity, vorticity, helicity, streamfunction, (reduced) pressure and kinetic energy, and enstrophy are non-dimensionalized with respect to the reference scales R , Ω_0^{-1} , $R\Omega_0$, Ω_0 , $R\Omega_0^2$, $R^3\Omega_0$, $R^2\Omega_0^2$, Ω_0^2 respectively.

2.2 Angular velocity distribution

As already mentioned in Bouffanais et al. [61] for the study of the lid-driven cubical cavity flow, imposing a given angular velocity distribution on the bottom end-wall of a cavity is not an easy task numerically. Indeed, imposing a constant angular velocity profile leads to a singularity (discontinuous behavior in the velocity boundary conditions) at the circular edge between the bottom end-wall and the tubular side-wall, see Fig. 1. Without adequate treatment, this discontinuous behavior will undermine the convergence and the accuracy of any numerical method in the vicinity of the lid. The same remedy as in the lid-driven cubical cavity problem in [61] is used here for the same reasons and with analogous justifications. A regularized angular velocity profile is employed by prescribing the following high-order polynomial expansion which vanishes

along its first derivatives on the circular edge

$$\boldsymbol{\Omega}(r, \theta, z = 0, t) = \Omega_0 \left[1 - \left(\frac{r}{R} \right)^{16} \right]^2 \mathbf{e}_z, \quad (4)$$

which leads to the following expressions in Cartesian coordinates of the components of the prescribed velocity field on the bottom end-wall

$$u(x, y, z = 0, t) = u_x(x, y, z = 0, t) = -y\Omega_0 \left[1 - \left(\sqrt{x^2 + y^2}/R \right)^{16} \right]^2, \quad (5)$$

$$v(x, y, z = 0, t) = u_y(x, y, z = 0, t) = +x\Omega_0 \left[1 - \left(\sqrt{x^2 + y^2}/R \right)^{16} \right]^2, \quad (6)$$

$$w(x, y, z = 0, t) = u_z(x, y, z = 0, t) = 0, \quad (7)$$

where $x = (r, \theta = 0)$ and $y = (r, \theta = \pi/2)$. This profile flattens very quickly near the circular edge ($r/R = 1, \theta, z/H = 0$) while away from it, it grows rapidly to a constant value Ω_0 of the angular velocity over a short distance. The highest polynomial degree of this distribution is 32. Such high-order polynomial expansions lead to steep velocity gradients in the vicinity of the circular edge of the bottom end-wall. The grid refinement, in terms of spectral element distribution near the disk will be presented in greater details in Sec. 3. One of the constraint in the grid design is to ensure the proper resolution of the lid velocity distribution by the spectral element decomposition.

2.3 Free-surface modeling

The analysis of a two-phase flow is based on the coupled hydrodynamics interactions between adjacent layers over a broad range of space and time scales. This analysis can be significantly simplified if the dynamics of the interface is almost entirely dependent—from the hydrodynamics and physico-chemistry viewpoints—on one phase, e.g. a liquid phase, and almost independent of the dynamics of the second phase, e.g. a gas phase. Based on this hypothesis, the surface is said to be *free*. Consequently, the two fluid phases can only exert constant normal stresses. Sarpkaya in his review entitled “Vorticity, free surface and surfactants” [62] gives a clear characterization and definition of a free surface: “Although, the exterior of a free surface is free from externally imposed shear, the interior is not necessarily free from the shear generated internally. In fact, surface deformations and contaminants give rise to surface-gradients and tangential stresses in the internal side of the bounding interface. From a mathematical viewpoint, a free surface means that the density and the viscosity of the upper fluid are zero and that the existence of a continuum above the interface is inconsequential. From a practical point of view, the free surface means that the dynamics of the continuum above the interface has negligible influence on the lower phase, i.e. a free surface is a simplifying approximation for an *almost free surface*.”

In the present study, the modeling of the interface between the fluids in the cylindrical cavity as a free surface is supplemented by an additional simplifying approximation: the free surface is supposed to remain flat and fixed all along the dynamic range of investigation. In general, the

dynamics of the free surface depends on the non-dimensional Froude number defined here as

$$\text{Fr} = \frac{R^2 \Omega_0^2}{gH}, \quad (8)$$

which measures the relative importance of the inertial effects compared to the stabilizing gravitational effects. Therefore, assuming a flat free surface corresponds mathematically to a Froude number identically zero. As a consequence and in consistency with the latter assumption, the axial component of the velocity $w = u_z$ needs to vanish at the free surface $z/H = 1$

$$w(x, y, z = H, t) = 0, \quad x^2 + y^2 \leq R^2, \quad (9)$$

thereby expressing the kinematic boundary condition at the free surface. This latter condition on the axial velocity w is to be supplemented with the stress-free condition at the free surface

$$\sigma_{ij}^* \hat{n}_j = -p \delta_{ij} \hat{n}_j + 2\nu D_{ij} \hat{n}_j = 0, \quad (10)$$

where $\hat{\mathbf{n}}$ is the local outward unit vector normal at the free surface, which in the present particular situation is the unit normal vector \mathbf{e}_z in the z -direction. Consequently, the stress-free condition (10) reduces to $\sigma_{i3}^* = \sigma_{iz}^* = 0$, $i = 1, 2, 3$ at $z = H$, and is explicitly stated as

$$\sigma_{13}^* = 2\nu D_{13} = 0, \quad (11)$$

$$\sigma_{23}^* = 2\nu D_{23} = 0, \quad (12)$$

$$\sigma_{33}^* = -p + 2\nu D_{33} = 0, \quad (13)$$

which under the zero-deformation condition (9), simplifies to

$$\left(\frac{\partial u}{\partial z} + \frac{\partial w}{\partial x} \right) = \frac{\partial u}{\partial z} = 0, \quad (14)$$

$$\left(\frac{\partial v}{\partial z} + \frac{\partial w}{\partial y} \right) = \frac{\partial v}{\partial z} = 0, \quad (15)$$

$$-p + 2\nu \frac{\partial w}{\partial z} = 0. \quad (16)$$

3 Computational approach

3.1 Space discretization

The Navier–Stokes equations (1)–(2), supplemented with the boundary conditions (3), (5)–(7), (9), (14)–(16), constitute the set of governing equations for this free-surface swirling flow to be discretized and ultimately solved. The numerical method treats Eqs. (1)–(2) within the weak Galerkin formulation framework. The spatial discretization uses Lagrange–Legendre polynomial interpolants. The reader is referred to the monograph by Deville et al. [63] for full details. The velocity and pressure are expressed in the $\mathbb{P}_N - \mathbb{P}_{N-2}$ functional spaces where \mathbb{P}_N is the set of polynomials of degree lower than N in each space direction. This spectral element method avoids the presence of spurious pressure modes as it was proved by Maday & Patera [64] and Maday et

al. [65]. The quadrature rules are based on a Gauss–Lobatto–Legendre (GLL) grid for the velocity nodes and a Gauss–Legendre grid (GL) for the pressure nodes. The spectral element grid used for all simulations is presented on Fig. 2, in the particular case $\Lambda = 1$. This mesh comprises 440 spectral elements distributed into 10 cylindrical layers of different heights, but all made of the same distribution of 44 spectral elements, see Fig. 2 (right). In order to resolve the boundary layer along the tubular side-wall, the Ekman shear layer above the rotating bottom end-wall and the surface shear layer below the free surface, the spectral elements are unevenly distributed as can be seen in Figs. 2. The choice of polynomial degree in the three space directions, defining the inner GLL and GL grid into each spectral element is deferred to Sec. 3.3. The essential Dirichlet

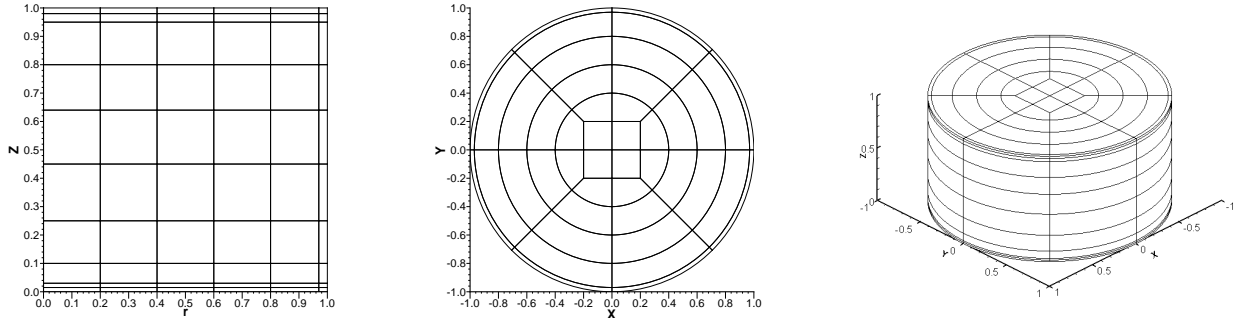


Fig. 2. Typical meshes view used throughout this study. Left: half-meridional grid. Center: spectral-element grid in any plane normal to the z -direction. Right: Three-dimensional grid comprising 10 cylindrical layers of nonuniform heights made of 44 spectral elements each. Case $\Lambda = 1$.

boundary conditions—homogeneous for \mathbf{u} on the tubular side-wall as expressed by Eq. (3), homogeneous for $w = u_z$ on the free surface as expressed by Eq. (9), and non-homogeneous for \mathbf{u} on the rotating bottom end-wall as expressed by Eqs. (5)–(7)—are embodied into the choice of test and trial functions chosen for the velocity field.

The stress-free condition (10) at the free surface, further expressed by Eqs. (14)–(16), appears as a homogeneous natural boundary condition in the weak Galerkin framework. This central point is discussed in detail and in a more general framework, in Bodard et al. [66], where a non-homogenous natural boundary condition is accounted for in the weak formulation of the problem. Based on this previous analysis, the treatment of the present stress-free condition at the free surface appears straightforward and is automatically incorporated into the weak formulation of the problem.

Borrowing the notation from Deville et al. [63], the semi-discrete Navier–Stokes equations resulting from space discretization are

$$\mathbf{M} \frac{d\mathbf{u}}{dt} + \mathbf{C}\mathbf{u} + \nu \mathbf{A}\mathbf{u} - \mathbf{D}^T \underline{p} = 0, \quad (17)$$

$$-\mathbf{D}\mathbf{u} = 0. \quad (18)$$

The diagonal mass matrix \mathbf{M} is composed of three blocks, namely the mass matrices M . The global vector \mathbf{u} contains all the nodal velocity components while \underline{p} is made of all nodal pressures. The matrices \mathbf{A} , \mathbf{D}^T , \mathbf{D} are the discrete Laplacian, gradient and divergence operators, respectively. The matrix operator \mathbf{C} represents the action of the non-linear term written in convective form $\mathbf{u} \cdot \nabla$, on the velocity field and depends on \mathbf{u} itself. The semi-discrete equations constitute

a set of non-linear ordinary differential equations (17) subject to the incompressibility condition (18).

3.2 Time integration

The time discretization of the semi-discrete set of governing equations (17)–(18) is the same as the one previously used in Bouffanais et al. [61] and Habisreutinger et al. [67]. We only briefly recall here the fundamentals of the method. The set of semi-discrete equations (17)–(18) is discretized in time using finite-difference schemes in a decoupled approach. The computation of the linear Helmholtz problem—corresponding to the stiffness matrix \mathbf{A} —is integrated based on an implicit backward differentiation formula of order 2, the nonlinear convective term—corresponding to the operator \mathbf{C} —is integrated based on a relatively simple extrapolation method of order 2, introduced by Karniadakis et al. [68], see Bouffanais [69] for full details.

3.3 Convergence tests

In order to demonstrate the spatial and temporal convergence of the simulation method, time series data have been analyzed, while varying separately the time-step Δt and the polynomial degree N of the GLL basis in each space direction, at the upper bound in Reynolds number $\text{Re} = 6000$, and with $\Lambda = H/R = 1$. As no experimental, nor numerical reference results are available for the present problem, three integral and one local quantities have been computed and compared. These three integral quantities are the total kinetic energy Q , enstrophy E and helicity \mathcal{H} of the flow, which definitions are recalled

$$Q = \frac{1}{2} \int_{\mathcal{V}} \mathbf{u} \cdot \mathbf{u} \, d\mathcal{V}, \quad (19)$$

$$E = \frac{1}{2} \int_{\mathcal{V}} \boldsymbol{\omega} \cdot \boldsymbol{\omega} \, d\mathcal{V}, \quad (20)$$

$$\mathcal{H} = \int_{\mathcal{V}} \mathbf{u} \cdot \boldsymbol{\omega} \, d\mathcal{V}. \quad (21)$$

The local quantity monitored is the axial velocity component $w = u_z$ at the point Π_0 of coordinates $(r/R = 0, z/H = 0.75)$, located along the cylinder axis. The location choice of this monitoring point is motivated by the study of Piva & Meiburg [50] for a very similar configuration but at smaller Reynolds numbers. They show that in the vicinity of this point, the axial velocity component reaches a local maximum. Given the relatively high Reynolds number of our benchmark simulation, a quite long transient—approximately 500 time units in Ω_0^{-1} units—is observed. Performing convergence tests involving a simulation time of the order of this transient time would simply be prohibitive. Consequently, it was chosen to assess the convergence after only 50 time units of simulations, which corresponds to the appearance of the first vortex-breakdown recirculation bubble in the fluid domain. First, the spatial convergence is assessed by varying the polynomial degree in the range $6 \leq N \leq 10$, while keeping the time-step values constant $\Delta t = 0.0025$. Results are reported in Table 1, and suggest that the spatial convergence is achieved using a polynomial degree $N = 8$ in all three space directions. This value is used for all

the direct numerical simulations presented in the sequel, except for one single case corresponding to the steady laminar case ($\Lambda = 1, \text{Re} = 900$), for which $N = 7$ is chosen.

N	Q	E	\mathcal{H}	$w(\Pi_0)$
6	2.02745e-02	2.11900e+01	1.29876e-01	3.28923e-03
7	2.08244e-02	2.18923e+01	1.33612e-01	3.40034e-03
8	2.19036e-02	2.37953e+01	1.66448e-01	3.81373e-03
9	2.19034e-02	2.37957e+01	1.66450e-01	3.81376e-03
10	2.19035e-02	2.37955e+01	1.66447e-01	3.81375e-03

Table 1

Spatial convergence analysis for the case ($\text{Re} = 6000, \Lambda = 1$) with $\Delta t = 0.0025 \Omega_0^{-1}$. Q in $R^3(R\Omega_0)^2$ units, E in $R^3\Omega_0^2$ units, \mathcal{H} in $R^4\Omega_0^2$ units, and w in $R\Omega_0$ units. Instant $t = 50\Omega_0^{-1}$.

Finally, the temporal convergence is assessed by varying the time-step, while keeping the polynomial degree constant at the value $N = 8$, in agreement with the earlier spatial convergence analysis. Results are reported in Table 2 below, and suggest that the temporal convergence is achieved using a time-step $\Delta t = 0.0025$. At a reduced Reynolds number compared to the one employed for this convergence analysis $\text{Re} = 6000$, greater values of the time-step have been chosen in relation with the more laminar nature of the flow without affecting the convergence of the simulations.

Δt	Q	E	\mathcal{H}	$w(\Pi_0)$
0.0050	2.08574e-02	2.14302e+01	1.36342e-01	3.49221e-03
0.0035	2.11896e-02	2.25311e+01	1.48303e-01	3.61923e-03
0.0025	2.19036e-02	2.37953e+01	1.66448e-01	3.81373e-03
0.0010	2.19034e-02	2.37960e+01	1.66446e-01	3.81379e-03

Table 2

Temporal convergence analysis for the case ($\text{Re} = 6000, \Lambda = 1$) with $N = 8$. Δt in Ω_0^{-1} units, Q in $R^3(R\Omega_0)^2$ units, E in $R^3\Omega_0^2$ units, \mathcal{H} in $R^4\Omega_0^2$ units, and w in $R\Omega_0$ units. Instant $t = 50\Omega_0^{-1}$.

4 Numerical simulations and results

4.1 General physical characteristics of the flow

The central characteristics of the flow in a closed cylindrical container with a bottom rotating end-wall is a large recirculation of the fluid. The features of the intense shear layer induced by the rotation of the bottom wall can be obtained from the analogy with the analysis by von Kármán for the flow generated by a spinning plate in an unbounded fluid domain, see the review by Zandbergen & Dijkstra [70] for full details. The rotation of the bottom wall has a suction effect on the fluid in the near-axis region and a pumping effect, while accelerating the fluid radially outwards in an Ekman shear layer of thickness $O(\text{Re}^{-1/2})$. In the framework of

our problem, this Ekman layer is bounded by the tubular cylinder side-wall, which forces the recirculation of the fluid in the upward direction along the side-wall, and towards the top wall. As the fluid approaches the curved corner, the radial velocity contribution to the kinetic energy is progressively transformed into an axial velocity contribution to the kinetic energy. It has been observed that the fluid turns and subsequently spirals upward along the tubular side-wall.

As mentioned in Sec. 1.3, replacing the fixed top solid wall with a free surface changes significantly the physics of the flow and the recirculation mechanisms. In absence of tangential stresses at the free surface, the boundary layer is replaced by a surface layer in the sense of Shen et al. [71, 72]. In addition, the inward spiraling fluid elements conserve their angular momentum at the free surface. When the related centrifugal force is large enough to balance the radial pressure gradient, the flow separates from the free surface and leads to the generation of a vortex breakdown bubble. The most striking difference between the flow patterns observed in the present open cylinder case and compared to the close cylinder one are the possible appearances of recirculation bubbles, which are generally attached to the free surface. Such flow patterns are simply impossible in presence of the no-slip condition imposed on the top wall in the closed cylinder case. More precisely, Iwatsu [58] determined 24 different flow states in the steady regime according to the meridional streamline patterns observed. Spohn et al. [8] summarized those flow states in a simplified bifurcation diagram in the (Λ, Re) space. Based on his extensive and comprehensive study, Iwatsu [58] came out with a more detailed and complex bifurcation diagram.

In subsequent studies, the stability of those steady axisymmetric flows were investigated. Young et al. [73], Miraghaie et al. [74], Lopez et al. [60], and Lopez & Marques [75] observed unstable azimuthal modes which are triggered at different values of the Reynolds number depending on the nature “shallow” ($\Lambda < 1$) or “deep” ($\Lambda > 1$) of the system. Valentine & Jahnke [56], Lopez [57], and Brøns et al. [53] associated the axisymmetry breakage to instability modes. These modes appear following a Hopf bifurcation which generally occurs at relatively high Reynolds number.

4.2 Cases studied

As mentioned in the previous sections, the physics of these free-surface swirling flows depends critically on the Reynolds number. Nevertheless, the height-to-radius aspect ratio Λ also has considerable impact on the observed nature of the flow. Very often, situations corresponding to extreme values of Λ have been studied, as they generally lead to simplified flow mechanisms. For instance, shallow systems ($\Lambda < 1$) are often referred to as “rotor-stator” configurations, in which the fluid is almost in a state of solid-body rotation. On the other hand, deep systems associated with large values of Λ , generate recirculation bubbles away from the free surface and generally on the cylinder axis. Consequently, systems corresponding to values of Λ close to the unity are intermediate in the sense that the physics of the flow observed is a complex combination of the general features reported for the shallow and deep systems.

The details related to the five cases considered in this article are summarized in Table 3. The primary focus is on the flow defined by $\text{Re} = 6\,000$ and $\Lambda = 1$, and corresponding to case (c). The value of the Reynolds number is intentionally set to a high value compared to previous studies—the highest to our knowledge, in order to obtain fields of a relative intensity at the free surface. The choice of the value of Λ follows the earlier comment on systems being intermediate

Case	Re	$\Lambda = H/R$	Time-step Δt	Time evolution	Vortex breakdown
(a)	900	1.0	0.0050	steady	one attached bubble
(b)	1 500	1.0	0.0050	steady	one attached toroidal bubble
(c)	6 000	1.0	0.0025	unsteady	complex dynamics
(d)	2 000	1/3	0.0040	steady	two long attached bubbles
(e)	2 000	3.0	0.0040	steady	one short detached bubble

Table 3

Parameters and characteristics of the cases considered. The time-step Δt is expressed in Ω_0^{-1} units.

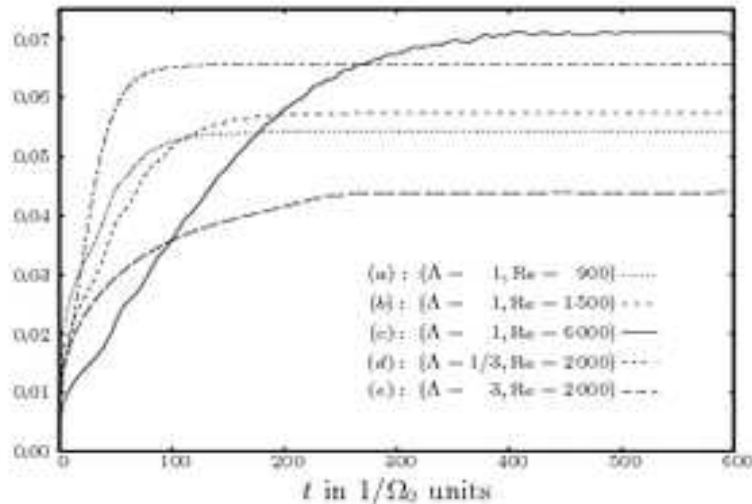


Fig. 3. Time history of the volume integral of the kinetic energy Q of the flow, in $R^5 \Omega_0^2$ units for cases (a)–(e).

between shallow and deep. This central case ($\Lambda = 1, \text{Re} = 6\,000$) is supplemented with four secondary cases described in Table 3. The study of those secondary flows is of prime importance for the understanding of the complex dynamics of the primary case ($\Lambda = 1, \text{Re} = 6\,000$).

In terms of initial conditions, the steady rotation is impulsively started from a quiescent fluid state for all cases presented in the sequel. At this point, it is worth noting the timescales of the evolution of these flows. Figure 3 displays the time history of the volume integral of the kinetic energy of the flow Q . For all cases except case (c), the flow reaches a steady state after a given time scale, which is, as expected, shorter for shallow systems. Case (c) leads to an unsteady flow which does not display any oscillatory evolution. The value of the Reynolds number for this case is large enough to produce a non-trivial evolution of the recirculation zones as will be seen in the sequel.

The time histories of the volume integral of the kinetic energy Q for the five cases (a) – (e) can be compared to the ones, reported in Bouffanais [69] for the closed swirling flow problem with $\Lambda = 2.5$, see Fig B.4. It should be noted that for a fixed value of Λ , the total kinetic energy Q of the flow decreases with the Reynolds number for the closed cylinder case, while it increases in the open cylinder case. This decreasing trend for Q in the closed cylinder case can easily be resolved by transposing the analysis given by Leriche & Gavrilakis [76] in their study of the closed lid-driven cubical cavity flow. Leriche & Gavrilakis argue that the most significant part

of the kinetic energy of the flow is contained in the viscous layer developing on the driving wall. Consequently, the total energy varies like the energy contained in this viscous layer which can approximately be expressed as $U_0^2 \mathcal{V} \text{Re}^{-1/2}$, where U_0 is the characteristic velocity of the driving wall and \mathcal{V} the volume of the cavity. Such argument and estimate can easily be transposed for the closed swirling flows, and explains the decreasing trend for Q with respect to Re . Furthermore this argument is confirmed by the measurements of the kinetic energy $Q(L_1)$ of the cylindrical layer of fluid L_1 located right above the spinning disk and of height $0.015H$, reported in Table 4. This thin layer of fluid which only represents 1.5% of the total volume of fluid, contributes for approximately 10% to the total kinetic energy of the flow. Concurrently, its contribution to the total kinetic energy of the flow decreases with the Reynolds number.

Re	$Q(L_1)$	$E(L_1)$	$E_z(L_1)$
900	7.42243e-03	3.04128e+00	3.99817e-01
1 500	7.05011e-03	4.46885e+00	4.03147e-01
6 000	5.71943e-03	1.18305e+01	4.25622e-01

Re	$Q(L_{10})$	$E(L_{10})$	$E_z(L_{10})$
900	3.88037e-04	6.14708e-03	5.99848e-03
1 500	5.47285e-04	9.04519e-03	8.25633e-03
6 000	1.21966e-03	6.43344e-02	2.00737e-02

Table 4

Measurements of the kinetic energy Q , enstrophy E , and enstrophy associated solely with the axial vorticity component E_z for the cylindrical layer L_1 comprised between $z = 0$ and $z = 0.015H$, and for the cylindrical layer L_{10} comprised between $z = 0.98H$ and $z = H$. Q in $R^3(R\Omega_0)^2$ units, E and E_z in $R^3\Omega_0^2$ units. Instant $t = 600\Omega_0^{-1}$.

On the contrary, a reverse trend is observed for the variations of Q with respect to Re in the open swirling flow. It therefore requires another physical justification. Nevertheless, the previous energetic argument associated with the viscous layer still holds for the viscous layer above the spinning disk and near the tubular side-wall in the open cylinder swirling flow. Below the surface at $z = H$, the viscous layer in the closed cylinder case is replaced by an intense shear layer. As mentioned in Sec. 2.3, in the present flat-free-surface problem, the axial vorticity ω_z is the only component of the vorticity field which is not vanishing at the free surface and it provides a measure of the internal shear at the free surface. The part E_z of the enstrophy associated with the axial vorticity component is measured in the cylindrical layer of fluid L_{10} , of height $0.02H$ and located below the free surface. Results are reported in Table 4 and clearly show a significant increase of E_z with respect to Re in the layer L_{10} , while it is almost constant in L_1 . These results allow us to infer that the shear layer below the free surface becomes more and more intense and energetic—see $Q(L_{10})$ — when increasing the Reynolds number. But this observed energetic trend of the free-surface shear layer is not the only factor responsible for counterbalancing the decreasing trend of the viscous layers. The internal structure of the free-surface layer is itself physically different as reported by Shen et al. [71, 72]. The so-called surface layer corresponds to a thin region adjacent to the free surface characterized by fast variations of the tangential vorticity components. This surface layer is caused by the dynamic zero-stress boundary conditions (10) at the free surface and lies inside a thicker blockage (or “source”) layer, which is due to the

kinematic boundary condition (9) at the free surface. The importance of the outer blockage layer is manifested mainly in the redistribution of the kinetic energy, i.e. in the increase of the kinetic energy of the tangential velocity components at the expense of the kinetic energy of the axial velocity component. This point is to be further discussed in Sec. 4.3.2, where a comprehensive comparison of the flow below the surface $z = H$ for the case (c) with a free surface and the equivalent closed case is given.

4.3 Physical description of flow states

4.3.1 Steady flows

As a first step, we present the two steady flows for $\Lambda = 1$ at $\text{Re} = 900$ and $1\,500$ corresponding to cases (a) and (b) respectively. Figure 4 displays the streamlines of these flows into any meridional plane. Both of these flows present a large axisymmetric vortex breakdown bubble attached to the free surface in agreement with the experimental results from Spohn et al. [8] summarized in their bifurcation diagram. These recirculation zones are characteristic of these swirling flows due to the conjugate effects of the centrifugal force and the overturning flow induced by the presence of the tubular side-wall. The central difference between the low-Reynolds-number cases (a) and (b) is the shape of the recirculation, which becomes toroidal after leaving the axis when the Reynolds number is increased from 900 up to 1 500. These results can be further validated by comparing them to the experimental results (dye visualizations) obtained by Piva for $\text{Re} = 1\,120$. Finally, case (a) ($\Lambda = 1, \text{Re} = 900$) has also been computed by Piva & Meiburg [50].

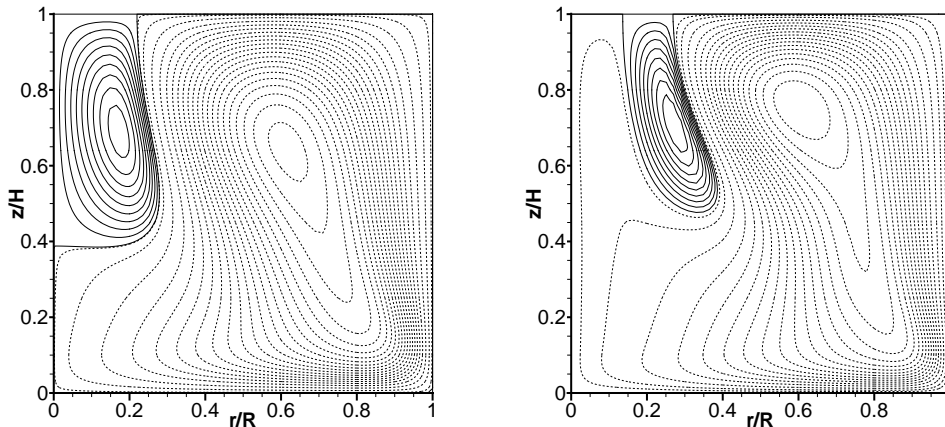


Fig. 4. Contours of streamlines in a meridional plane, case $\Lambda = 1$. Left: case $\text{Re} = 900$; Right: case $\text{Re} = 1\,500$. The 30 contours are non-uniformly spaced for visualization purposes, 20 equally-spaced negative contours and 10 equally-spaced positive contours for $\text{Re} = 900$ and $\text{Re} = 1\,500$.

As a second step, the contours of the radial, azimuthal and axial velocity components in any meridional plane are given in Fig. 14. These data are supplemented with the contours of the axial component of the angular momentum $\Gamma = ru_\theta$ still in Fig. 14, extreme right column. The interest for Γ lies in the fact that it plays the role of a streamfunction for the part of the velocity field comprised in any meridional plane, see Bragg & Hawthorne [77] and Keller [78] for full details. Therefore, the contours of Γ deliver the intersection of vortex surfaces with the

corresponding meridional plane where they are drawn, and as such provide us with the local direction of the meridional vorticity field. One can notice from the velocity components and axial angular momentum component that the meridional structure of these flows is far from being trivial. It consists of an intense boundary layer above the spinning bottom end-wall that is turned into the interior by the presence of the tubular side-wall, forming a shear layer having a jet-like velocity profile in the azimuthal direction. The contour lines of the axial component of the angular momentum shown in Fig. 14 (extreme right column) simply represent the vortex lines, which all emanate from the rotating disk; the structure of the shear layer is apparent. It is worth noting here that the vortex lines distribution at their origin varies like r^2 . As a consequence of the regularized profile of angular velocity of the rotating disk—see Sec. 2.2, this distribution in r^2 is slightly affected in the vicinity of $r = R$. This regularization of this profile has the advantage of preventing the appearance of vortex lines terminating at the circular corner ($r = R, z = 0$). The overturning nature of these flows is also apparent in the vicinity of the tubular side-wall, which is the vortex surface corresponding to $\Gamma = 0$, together with the cylinder axis. As non-zero azimuthal velocities are possible at the free surface, vortex lines emanating from the rotating end-wall have the option of terminating orthogonally to the free surface. This observation is one of the major difference with the closed cylinder swirling flow where all vortex lines have to terminate in the corner. Furthermore, the termination of vortex lines at the free surface is responsible for the possibility of having vortex breakdown bubbles being attached to the free surface as observed in Fig. 4. A careful analysis of Fig. 14 (extreme right column) reveals that one vortex line marks the limit between an inner region comprising only vortex lines terminating at the free surface, and an outer region, where they terminate near the circular corner, like in the closed cylinder case. In summary, it appears that the main effect of this overturning flow is to bring high-angular-momentum fluid towards the cylinder axis.

The results for case (a) ($\Lambda = 1, \text{Re} = 900$) presented in Fig. 4 (left) and Fig. 14 (top row) show a qualitative good agreement with the numerical results of Piva & Meiburg [50]. The differences related to the features of the recirculation bubbles for cases (a) and (b) have been discussed earlier. One can notice in Fig. 14 (two first left columns), that the thicknesses of the intense radial velocity layer as well as the axial wall jet are reduced when the Reynolds number is increased from 900 to 1 500, as expected. The contours of the axial velocity component reveal that the downward-directed flow induced by the suction effect of the Ekman layer, is more intense at higher Reynolds number. In addition, the region of the flow where $w = u_z$ has a negative extremum tends to move closer to the free surface when increasing Re. Regarding the vortex lines shown in the extreme right column, their bending towards the cylinder axis is more pronounced at the higher Reynolds number of 1 500. In relation with the previous analysis, this latter observation highlights the fact that more high-angular-momentum fluid is brought towards the axis when increasing Re.

As mentioned in Sec. 4.2, our primary interest lies in case (c) ($\Lambda = 1, \text{Re} = 6\,000$), thereby justifying the study of cases (a) and (b), having the same aspect ratio Λ but corresponding to laminar cases. Nevertheless, the study of cases (d) and (e), which both correspond to “extreme” cases in terms of height-to-radius aspect ratio, illustrate some essential features of the open swirling flow. In case (c) some of these features may prevail only in specific regions of the flow as it corresponds to an intermediate case between a shallow system characterized by case (d) and a deep system characterized by case (e). These features are as follows:

- solid-body rotation of the inner core region, predominantly for small Λ ;
- radial jet of angular momentum at the free surface;
- lateral jet-like shear layer along the tubular side-wall;

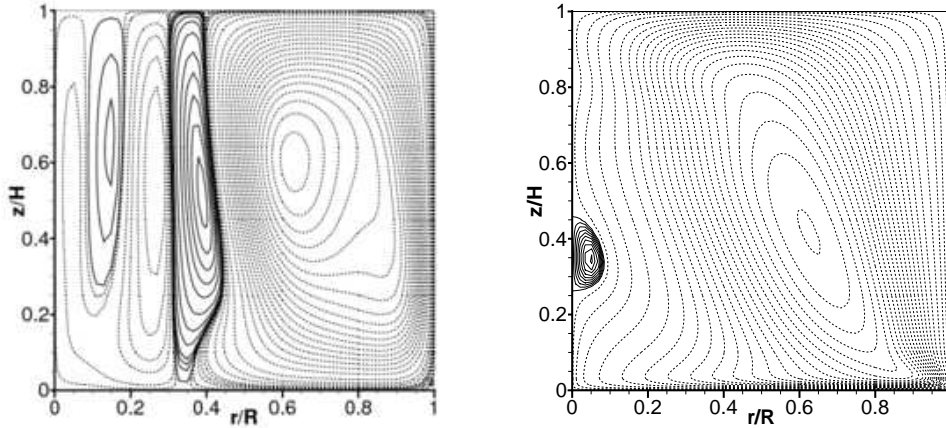


Fig. 5. Contours of streamlines in a meridional plane. Left: case (d) : ($\Lambda = 1/3, \text{Re} = 2000$); Right: case (e) : ($\Lambda = 3, \text{Re} = 2000$). The 30 contours are non-uniformly spaced for visualization purposes, 20 equally-spaced negative contours and 10 equally-spaced positive contours for (d) and (e) .

The very different flow patterns developed by both cases (d) and (e) are highlighted by the very distinctive streamlines shown in Fig. 5. The shallow case (d) yields two vortex breakdown bubbles, which are off the cylinder axis while remaining attached to the free surface. The recirculation is more intense in the largest bubble, which is elongated enough to produce a recirculation of the fluid from the free surface all the way down to the rotating disk, and so forth. Consequently, this elongated bubble completely separate the outer region of the flow ($r/R \geq 0.5$) from the inner core, where the second less intense, vortex breakdown occurs. Comparatively, the recirculation in case (e) is fairly limited. A vortex breakdown still occurs in this case, leading to the formation of a small on-axis bubble, which is detached from the free surface. One can notice from the bending of the streamlines near the axis at the height $z/H = 0.8$, that another vortex breakdowns is in preparation—compare this effect to the similar effect on the streamlines prior the vortex breakdown in the closed swirling flow at $\text{Re} = 1900$, see Bouffanaï [69].

The shallow system (d) ($\Lambda = 1/3, \text{Re} = 2000$) possesses some very distinctive features as can be seen in Fig. 15 (top row). The vortex lines for $r/R < 0.4$ being aligned with the rotation axis, one can easily conclude that the flow is essentially in solid-body rotation in this inner core region of the cavity. The meridional flow in this inner part of the cavity has a very weak intensity as attested by the values close to zero of the contours of the axial and radial velocity components—solid contour lines are positive and negative contour lines being dashed. In contrast, for $r > 0.4$ the primary recirculation of the flow is intense and predominates. The vortex lines bending is limited to this region and again is at the origin of the vortex breakdown appearing near $r/R = 0.4$. The boundary layer on the rotating disk is limited to the region $r/R > 0.5$ and the internal jet-like shear layer close the tubular side-wall has a structure quite different from the cases with $\Lambda = 1$. Indeed in this shear layer, the axial velocity is relatively intense all along the tubular side-wall, unlike cases (a) , (b) and (e) , where the axial velocity u_z decreases rapidly with z/H . This observation is easily explained by the shorter height in the case studied, but has several considerable consequences on the flow itself. A more intense wall-jet implies a

more intense angular momentum jet at the free surface, which facilitates the vortex breakdown phenomena. The intense angular momentum free-surface jet produces an elongated recirculation bubble located as seen earlier, around $r/R = 0.4$. In this elongated bubble, the axial velocity field is globally positive, thereby producing an effect similar to the jet-like shear layer near the tubular side-wall. In turn it generates a secondary angular momentum free-surface wall jet responsible for the second vortex breakdown.

Increasing the height-to-radius aspect ratio to $\Lambda = 3$, modifies considerably the flow dynamics as can be seen in Fig.15 (bottom row). It seems clear from the previous analysis for the shallow case (*d*), that the influence of the free surface on the flow is more important when Λ is small. The proximity between the driving disk, which generates the primary flow and the free surface with its specific boundary conditions, leads to the complex flow dynamics earlier explained. Conversely, for large values of Λ the important distance between the spinning disk and the free surface is so important that it significantly reduces the effect of the presence of the free surface. The flow pattern presents *in fine* a structure very similar to the flow pattern observed in the closed cylinder swirling flow, except very close to the free surface. As mentioned earlier the recirculation bubble itself is fairly small and located on the cylinder axis likewise in the closed cylinder case. Finally, it is worth adding that the region of solid-body rotation is almost completely eliminated. Even the closest-to-the-axis vortex lines present some bending.

As a brief conclusion of the previous study of the steady and laminar free surface swirling flows, it appears that the choice $\Lambda = 1$ for the height-to-radius aspect ratio of the cavity in presence of a free surface, ensures us to deal with a complex flow dynamics. Different mechanisms are in competition in different regions of the cavity, and in the end make the cases with $\Lambda = 1$ physically more challenging and more interesting. This conclusion—valid in presence of a free surface—stops being valid for the closed cylinder swirling flow, and thereby explains the focus in the literature on cases with $\Lambda \geq 2$.

4.3.2 Unsteady flow

For sufficiently small Reynolds number and irrespective of Λ , the basic flow state is stable. As noted by Lopez et al. [60], when Re is increased, the basic flow state loses stability via a variety of Hopf bifurcations. It is worth noting that when Re tends to infinity, the stream surfaces and vortex surfaces—giving the streamlines and vortex lines by intersection with a meridional plane—must coincide. At this point, the presence of a flat free surface poses problem because of the constraint of having orthogonal streamlines and vortex lines on it. This apparent paradox is unraveled by simply letting the free surface move. Nevertheless, we know from the experiments carried out by Spohn et al. [8, 22], that even at a $Re = 6\,000$ the tangential flow is extremely intense compared to the normal one, leading to small free-surface deformations. It is very likely that these small amplitude deformations are not sufficient to solve our apparent paradox. At low Reynolds number, like those of cases (*a*), (*b*), (*d*), and (*e*), the viscosity acts on the velocity field to allow the latter condition of orthogonality to be fulfilled. But when the Reynolds number is increased, the action of viscosity and the limited deformation of the free surface are not sufficient to bring back the orthogonality of the two sets of lines. Therefore, the flow must either lose its axisymmetry or become unsteady in order to allow to drop the orthogonality condition. The experiments by Spohn et al. [8] suggest that the open swirling flow first go through the unsteady path.

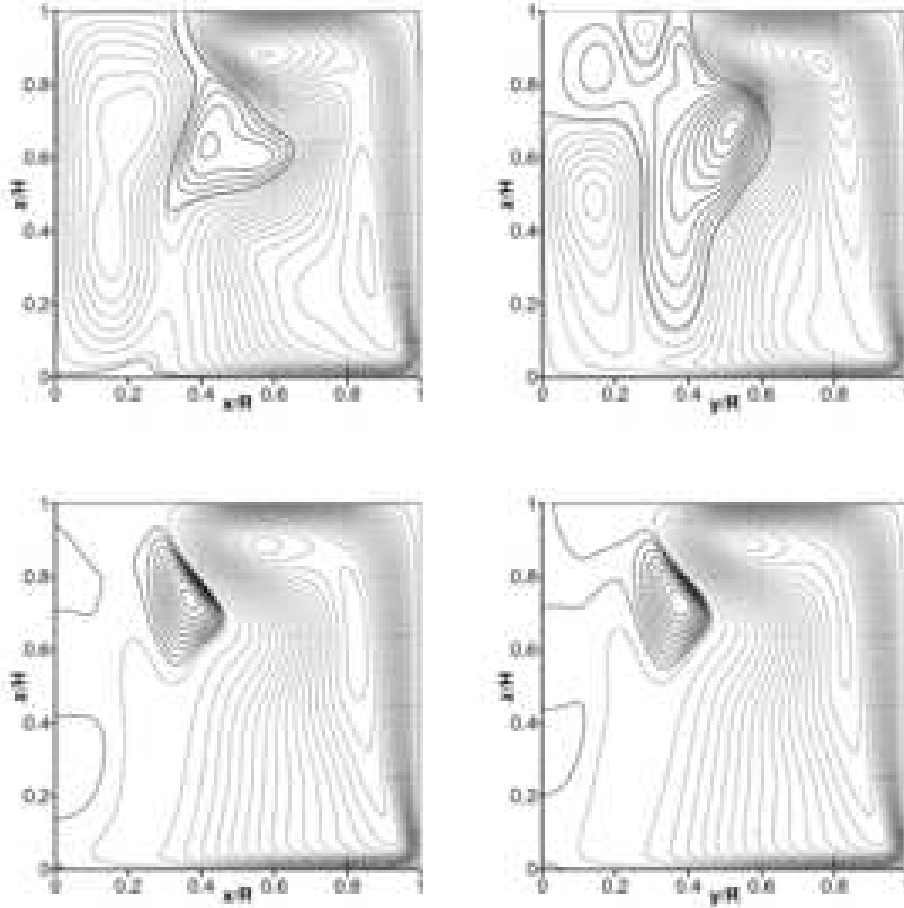


Fig. 6. Contours of streamlines in two orthogonal meridional planes, case $\Lambda = 1$ and $\text{Re} = 6000$. Top row: instantaneous flow; Bottom row: mean flow. Left column: meridional plane $y/R = 0$; Right column: meridional plane $x/R = 0$. The 30 contours are non-uniformly spaced for visualization purposes, 20 equally-spaced negative contours and 10 equally-spaced positive contours.

In this section, the study is focused on the unsteady swirling flow corresponding to case (c) = ($\Lambda = 1, \text{Re} = 6000$). To our knowledge, such transitional regime at this relatively high Re has never been investigated nor reported in the literature. At this Reynolds number the loss of axisymmetry in this flat-free-surface case is evident from the observation of the contours of streamlines in Fig. 6 (top row). As the flow is unsteady, these recirculation bubbles are instantaneous and correspond to a flow sample taken in the statistically-steady regime for $t > 600$ in Ω_0^{-1} units, see Fig. 3. The streamlines of this flow sample are represented in two orthogonal meridian planes corresponding to $y/R = 0$ and $x/R = 0$, in Fig. 6 (top row). Once again, the loss of axisymmetry appears clearly from the complex and nonaxisymmetric structure of the recirculation bubbles. Compared to the laminar and steady cases (a) and (b), the recirculation bubbles have their own dynamics and evolution. In a common approach to such unsteady problems, this complex dynamics is analyzed by the means of an averaging process, which is supplemented with an analysis of instantaneous flow samples equally-spaced in time. The mean flow is obtained by averaging 500 flow samples corresponding to successive flow states extracted every 0.25 times units (or equivalently every 100 iterations). Subsequently, the root-mean-square (rms) fluctuations of flow fields are calculated using the same extracted flow samples and the mean flow field

obtained earlier.

The streamlines associated with the mean flow are shown in Fig. 6 (bottom row). The streamlines of the mean flow reveal the existence of a toroidal recirculation bubble, located off the cylinder axis and more surprisingly detached from the free surface. The toroidal shape and off-axis location of the mean recirculation bubble is in agreement with the increased-Re trend observed with cases (a) and (b) in Sec. 4.3.1. Regarding the detachment from the free surface of the mean bubble, it is more relevant here to notice that the instantaneous bubbles are still attached to the free surface. More precisely, one may notice two points:

- in the meridional plane $y/R = 0$, a small recirculation zone appears attached to the rotating disk for $r/R \simeq 0.2$;
- in the meridional plane $x/R = 0$, the recirculation bubble is stretched from the free surface $z/H = 1$ down to $z/H = 0.15$, in a radial position $r/R \simeq 0.4$.

These two observations remind the streamline patterns described in the case (d) = ($\Lambda = 1/3, \text{Re} = 2000$), with a long bubble stretching from the free surface down to the driving disk. The previous analysis is further confirmed by the contours of the three velocity components and of the axial angular momentum for both an instantaneous flow sample and the mean flow, presented in Fig. 16, in the meridional plane $x/R = 0$. A careful analysis of the vortex lines for the instantaneous flow sample shows a bending in the whole meridian plane. This bending is very significant in the region $0.3 \leq r/R \leq 0.8$ and $0.4 \leq z/H \leq 1$, which corresponds to the limit between the primary recirculation of the flow and the secondary recirculation bubble. On the contrary, the vortex lines structure of the mean flow is as expected much more regular. The inner core region of the flow $r/R \leq 0.4$ displays a state of solid-body rotation. For both the instantaneous and mean flow, the jet-like shear layer along the tubular side-wall is turned into the interior of the flow by the free surface. Compared to the previous cases (a), (b), (d), (e), and also the closed swirling flow ($\Lambda = 1, \text{Re} = 6000$) in Bouffanais [69], the structure of this shear layer at $\text{Re} = 6000$ reveals the presence of an intense radial jet of angular momentum at the free surface.

The fluctuations of the flow with respect to its mean state have been calculated with the same flow samples as before. It should be noted that the fluctuation level corresponds to less than 5% of the maximal intensity of the respective mean flow fields. Despite the relatively low level of fluctuation encountered, these fluctuations are very localized in space as can be seen in Fig. 17. Similarly to the mean flow fields, the rms fluctuations of the velocity field and of Γ appear to be slightly nonaxisymmetric. All the three velocity components present a noticeable level of fluctuation near the free surface for radii close to 0.4. In this region, the free-surface radial jet of angular momentum reaches the inner flow, which is solid-body rotation. These fluctuations are therefore located in the vicinity of the stagnation point where the vortex breakdown is initiated. The rms-fluctuations of the vortex lines, i.e. Γ , are the highest in the corner region between the free surface and the tubular side-wall. It is in this corner, where the shear layer is turned into the interior by the presence of the free surface.

4.4 One-dimensional momentum budgets

This section is devoted to the careful analysis of the momentum balance for the radial, azimuthal and axial components. This study is performed along different radial and axial lines within the cavity. It is of interest to determine the predominant physical terms, which are responsible for the complex flow dynamics depicted in the previous sections. As noticed in these previous sections, the structure of the flow in the inner core region is far different from the one close to the tubular side-wall. Similarly, the flow above the rotating driving disk has properties, which are not comparable to the ones below the flat free surface. For the sake of conciseness, this momentum balance analysis is limited to cases (a) – (c) for which $\Lambda = 1$.

4.4.1 General considerations

The numerical integration of the Navier–Stokes equations using the spectral element method as described in Sec. 3, is performed in Cartesian coordinates (x, y, z) for the velocity components (u, v, w) . Nevertheless, the axisymmetric nature of the container and of the boundary conditions imposed to the flow suggests the use of cylindrical coordinates. Indeed, the different physical terms involved in the momentum equation represented here by the Navier–Stokes equations—nonlinear advective term, viscous strain, pressure gradient, etc.—are better apprehended when expressed in cylindrical coordinates. Accordingly, all vectors and physical terms are recast as functions of (r, θ, z) , and for instance the velocity components are (u_r, u_θ, u_z) .

The complete expression of the momentum equations in cylindrical coordinates reads

$$\frac{\partial u_r}{\partial t} + u_r \frac{\partial u_r}{\partial r} + \frac{u_\theta}{r} \frac{\partial u_r}{\partial \theta} - \frac{u_\theta^2}{r} + u_z \frac{\partial u_r}{\partial z} = -\frac{\partial p}{\partial r} + \frac{1}{\text{Re}} \left[\frac{\partial}{\partial r} \left(\frac{1}{r} \frac{\partial (r u_r)}{\partial r} \right) + \frac{1}{r^2} \frac{\partial^2 u_r}{\partial \theta^2} - \frac{2}{r^2} \frac{\partial u_\theta}{\partial \theta} + \frac{\partial^2 u_r}{\partial z^2} \right], \quad (22)$$

$$\frac{\partial u_\theta}{\partial t} + u_r \frac{\partial u_\theta}{\partial r} + \frac{u_\theta}{r} \frac{\partial u_\theta}{\partial \theta} + \frac{u_r u_\theta}{r} + u_z \frac{\partial u_\theta}{\partial z} = -\frac{1}{r} \frac{\partial p}{\partial \theta} + \frac{1}{\text{Re}} \left[\frac{\partial}{\partial r} \left(\frac{1}{r} \frac{\partial (r u_\theta)}{\partial r} \right) + \frac{1}{r^2} \frac{\partial^2 u_\theta}{\partial \theta^2} + \frac{2}{r^2} \frac{\partial u_r}{\partial \theta} + \frac{\partial^2 u_\theta}{\partial z^2} \right], \quad (23)$$

$$\frac{\partial u_z}{\partial t} + u_r \frac{\partial u_z}{\partial r} + \frac{u_\theta}{r} \frac{\partial u_z}{\partial \theta} + u_z \frac{\partial u_z}{\partial z} = -\frac{\partial p}{\partial z} + \frac{1}{\text{Re}} \left[\frac{1}{r} \frac{\partial}{\partial r} \left(r \frac{\partial u_z}{\partial r} \right) + \frac{1}{r^2} \frac{\partial^2 u_z}{\partial \theta^2} + \frac{\partial^2 u_z}{\partial z^2} \right], \quad (24)$$

where successively appears, the velocity time derivative, the nonlinear advective term, the pressure gradient and the viscous strain. The central objective of this study is to compare the relative importance of some of these terms along different lines. Equation (22) (resp. (23)) represents the momentum balance in the radial (resp. azimuthal) direction, and is analyzed along four radial lines at four different heights $z/H = 0.03, 0.64, 0.95, 1$, ranging from right above the rotating disk up to the free surface. Equation (24) represents the momentum balance in the axial direction, and is analyzed along three different axial vertical lines at three radial positions $r/R = 0.08, 0.48, 0.98$, ranging from near the cylinder axis to near the tubular side-wall.

For the sake of simplicity, some of the terms appearing in (22)–(24) are identified and denoted specifically in Table 5. In the sequel, the various graphs reporting the variations of these terms will use this nomenclature.

Name	Expression	Name	Expression	Name	Expression
NLr1	$-u_r \frac{\partial u_r}{\partial r}$	NLt1	$-u_r \frac{\partial u_\theta}{\partial r}$	NLa1	$-u_r \frac{\partial u_z}{\partial r}$
NLr2	$+\frac{u_\theta^2}{r}$	NLt2	$-\frac{u_r u_\theta}{r}$	NLa2	$-u_z \frac{\partial u_z}{\partial z}$
NLr3	$-u_z \frac{\partial u_r}{\partial z}$	NLt3	$-u_z \frac{\partial u_\theta}{\partial z}$	PGa	$-\frac{\partial p}{\partial z}$
PGr	$-\frac{\partial p}{\partial r}$	VSt1	$\frac{1}{\text{Re}} \left[\frac{\partial}{\partial r} \left(\frac{1}{r} \frac{\partial(r u_\theta)}{\partial r} \right) \right]$	VSa1	$\frac{1}{\text{Re}} \left[\frac{1}{r} \frac{\partial}{\partial r} \left(r \frac{\partial u_z}{\partial r} \right) \right]$
VSr	$\frac{1}{\text{Re}} \left[\frac{\partial}{\partial r} \left(\frac{1}{r} \frac{\partial(r u_r)}{\partial r} \right) + \frac{\partial^2 u_r}{\partial z^2} \right]$	VSt2	$\frac{1}{\text{Re}} \left(\frac{\partial^2 u_\theta}{\partial z^2} \right)$	VSa2	$\frac{1}{\text{Re}} \left(\frac{\partial^2 u_z}{\partial z^2} \right)$

Table 5

Name definitions of different terms appearing in the momentum budget equations (22)–(24).

4.4.2 Steady flows

As discussed in Sec. 4.3.1, the steady swirling flows are also fully axisymmetric. The first-order time derivative of the velocity fields is identically zero in Eqs. (22)–(24). The axisymmetric property makes the velocity field independent of the azimuthal angle θ , and consequently all partial derivatives with respect to this variable vanish. Therefore, the balance in the momentum equation solely involves the terms described in Table 5.

As a first step, the momentum balance in the radial direction is presented in Fig. 7 for case (a) (left column) and case (b) (right column). At the free surface $z/H = 1$ (top row), the viscous terms are insignificant, and the flow is driven by the radial pressure deceleration, which is mainly counterbalanced by the centrifugal acceleration $\text{NLr2} = u_\theta^2/r$ and to a certain extent by NLr1 . This analysis at the free surface still holds below the free surface at $z/H = 0.94$ and at $z/H = 0.64$. At this latter height, both the radial pressure deceleration and the centrifugal acceleration NLr2 have a lower magnitude than at the free surface but their magnitude is less localized than at the free surface. As expected, above the disk, at $z/H = 0.03$, all the terms have a higher magnitude and the momentum balance is more complex as only one single term NLr3 does not really contribute to the balance. The centrifugal acceleration NLr2 keeps its predominant position, but its maximum is now shifted towards the outer radial region, which corresponds to the region of highest angular momentum $0.8 \leq r/R \leq 1$. The other acceleration term NLr1 becomes relatively important. Both of these acceleration terms are counterbalanced by the radial pressure gradient and now also by the viscous strain. The importance of the viscous strain at this height $z/H = 0.03$ can easily be understood, as we are located in the viscous layer generated by the motion of the disk. One may add that in the inner core region of the flow, say $r/R < 0.15$, the linear trend observed for both the centrifugal acceleration and the pressure deceleration are well-known features of a flow in solid-body rotation, as observed with the vertical vortex lines in Fig. 14 (extreme right column).

The evolution of those momentum balances along radial lines at different heights does not really change when increasing Re from 900 up to 1500. But some noticeable trends are observable. For instance, even if the viscous strain does not play a central role at the free surface, it is worth noting that its effect is increased with Re while conversely it is decreased when getting closer

to the rotating bottom end-wall.

As a second step, we aim at analyzing the momentum balance in the azimuthal direction along radial lines at the same different heights as before. The results are presented in Fig. 8 for case (a) (left column) and case (b) (right column). It is important to note at this point that the two terms $NLt1$ and $VSt1$ involve partial derivatives with respect to the radial variable r . Given the fact that our solution is continuous and first-order differentiable within a spectral element and only continuous at the element edges, one expects some slight unphysical deformations of the plots associated with these two terms. Along the radial lines of interest, the spectral element edges are located at $r/R = 0.2, 0.4, 0.6, 0.8, 0.97$. As a consequence, some rapid variations of the terms $VSt1$ and $NLt1$ are going to be simply disregarded in the coming discussions.

A rapid glance at all the plots in Fig. 8 allows to conclude that the importance of the azimuthal momentum transfers resides in the near bottom end-wall region. The magnitude of all terms is over ten times smaller at $z/H = 0.64, 0.95, 1$, compared to $z/H = 0.03$. Given the solid-body rotation in the inner core region of the flow $r/R < 0.15$, most of the terms are vanishing small—excluding the unphysical values of $VSt1$.

At $z/H = 0.03$, one can notice the vigorous action of the viscous strain term $VSt2$ which literally drives the fluid in the viscous Ekman layer. This driving viscous term is being compensated by the convective terms $NLt1$ and $NLt3$, and by the Coriolis term $NLt2$. As one gets closer to the corner between the rotating disk and the tubular side-wall, say $r/R \geq 0.8$, the interplay between the various terms is being reversed. The term $VSt2$, which is driving the fluid in the inner region of the cavity is now a dissipative term in the jet-like shear layer. Conversely, the convective term $NLt1$ becomes large and is driving the fluid in the shear layer. Very close to the tubular side-wall, this term starts being counterbalanced by the second viscous term $VSt1$.

The viscous driving effect of the term $VSt2$ becomes insignificant at $z/H = 0.64$, but when z/H is increased, $VSt2$ starts growing again to reach a local maximum value at the free surface, but with a magnitude slightly smaller than the two other nonlinear convective terms $NLt1$ and $NLt2$. Close to the free surface and at the free surface, the flow is primarily driven by the Coriolis term $NLt2$ together with the viscous term $VSt2$. Their global action is counterbalanced by the nonlinear convective term $NLt1$. This momentum balance at the free surface in the outer region $r/R \geq 0.4$ reflects the central effect of the free-surface jet of angular momentum. Again the viscous effects are more intense at the free surface when Re is increased from 900 to 1500, despite the presence of the kinematic viscosity term $1/Re$ in their definitions.

As a last step for these two steady flows (a) and (b), we investigate the momentum transfer in the axial direction, but now along three different vertical lines corresponding to three different radii $r/R = 0.08, 0.48, 0.98$. The graphs for the five different terms involved are reported in Fig. 9. We start from the top row, which is associated with the results for $r/R = 0.98$ in the jet-like shear layer and which present the highest magnitudes of all radii considered. The lack of axial momentum transfers is clearly visible in the region $z/H \geq 0.4$ and even inexistent at the free surface. Conversely, in the corner between the rotating bottom end-wall and the tubular side-wall the flow is driven by the axial pressure gradient, and to some extent by the two nonlinear terms $NLa1$ and $NLa2$ independently. The viscous term $VSa1$ is primarily responsible for counterbalancing the driving pressure effects. The second viscous term $VSa2$ has a less important effect in terms of magnitude but is driving very close to the disk (viscous Ekman

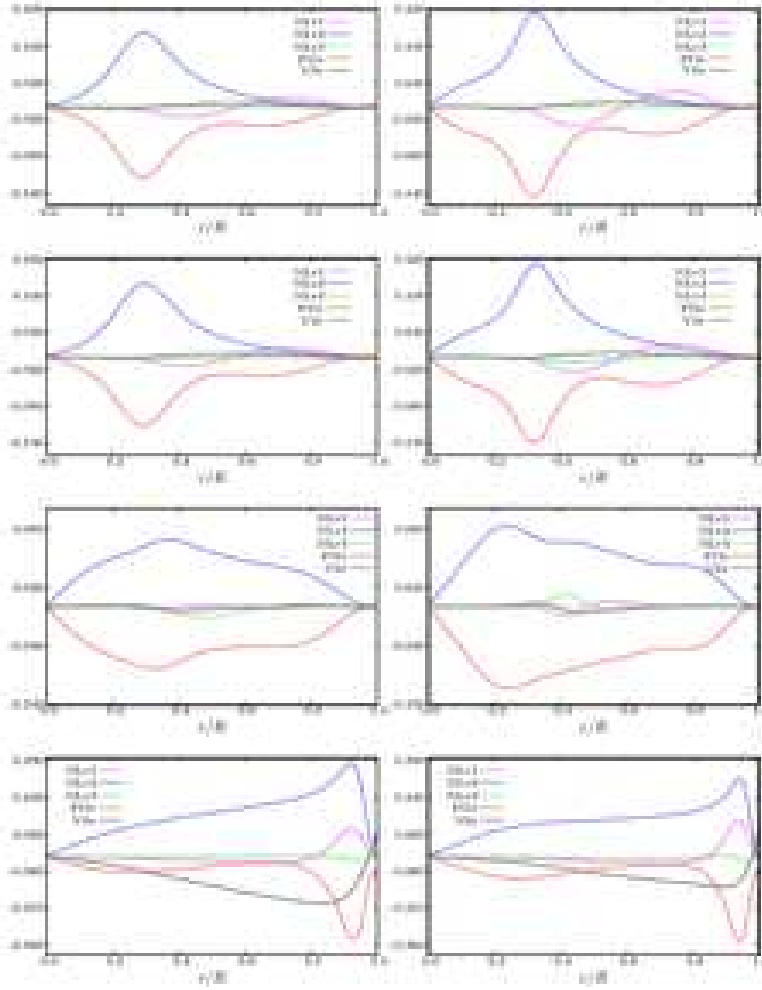


Fig. 7. Momentum balance in radial direction plotted along horizontal radial lines at four different vertical positions. First row: $z/H = 1$; second row: $z/H = 0.95$; third row: $z/H = 0.64$; fourth row: $z/H = 0.03$. Left column: case $Re = 900$; Right column: case $Re = 1500$. Case $\Lambda = 1$. The terminology refers to Tab. 5.

layer), when z/H is increased it becomes dissipative as we are out of the Ekman layer but within the wall-jet shear layer.

Near the medium radial position $r/R = 0.48$, the axial momentum transfers near the free surface show the relative importance of the two nonlinear terms $NLa1$ and $NLa2$, which are driving the fluid against the axial pressure gradient, which is negative as a consequence of the kinematic boundary condition imposing a vanishing axial velocity component at the free surface.

Near the cylinder axis, for $r/R = 0.08$, the axial momentum transfers are limited and relatively simples. Nonlinear convective effects seem almost insignificant and the axial component of the flow is obtained from the balance between the axial pressure gradient and the two viscous terms: $VSa2$ in the bottom of the cavity and $VSa1$ in the top of the cavity.

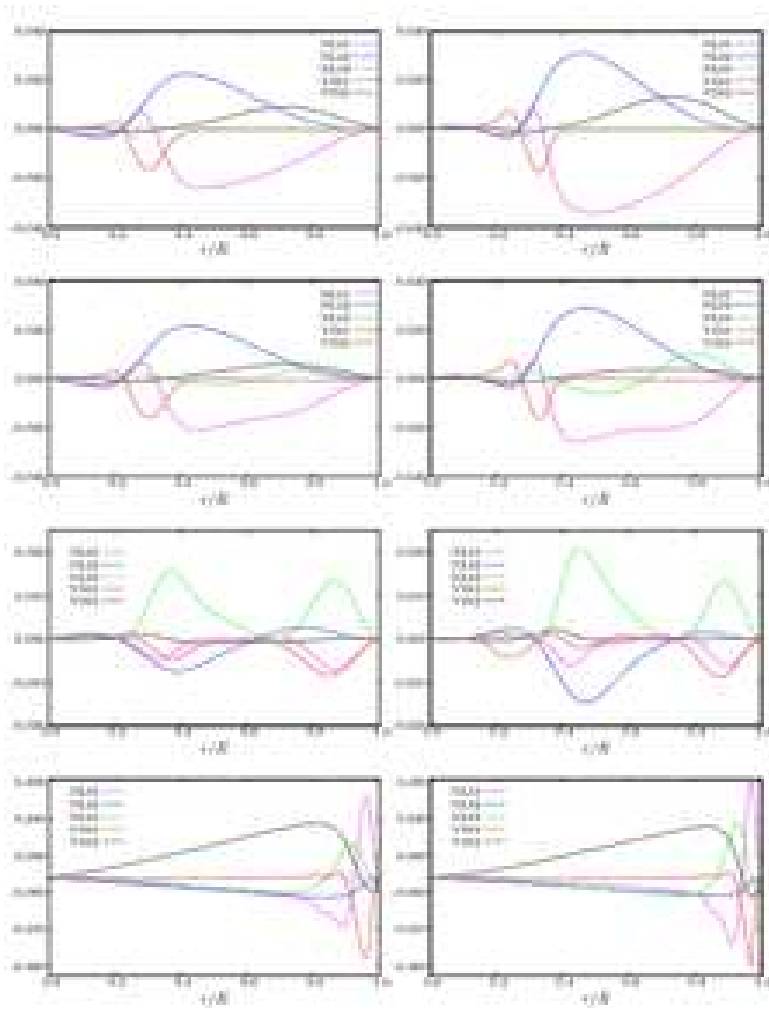


Fig. 8. Momentum balance in azimuthal direction plotted along horizontal radial lines at four different vertical positions. First row: $z/H = 1$; second row: $z/H = 0.95$; third row: $z/H = 0.64$; fourth row: $z/H = 0.03$. Left column: case $Re = 900$; Right column: case $Re = 1500$. Case $\Lambda = 1$. The terminology refers to Tab. 5.

4.4.3 Unsteady flow

The momentum balance analysis developed in the previous section for the two steady flows (a) and (b) cannot be directly transposed to the unsteady case (c). The two reasons for that are first the unsteady character requiring to account for the first-order time derivative $\partial \mathbf{u} / \partial t$. The second reason is the loss of axisymmetry of case (c) imposing to account for all the terms involving a partial derivative with respect to θ in Eqs. (22)–(24). One can overcome the issue associated with $\partial \mathbf{u} / \partial t$ by performing the analysis on the mean flow, which is obtained from the statistically steady regime. On the other hand, the momentum equations for the mean flow involve the Reynolds stress terms, expressing the influence of the fluctuating velocity field onto the dynamics of the mean field. Despite all these considerations and issues, we have deliberately omitted the terms involving derivatives with respect to the time and to the azimuthal coordinate, and we have calculated the values of the terms in Table 5 on the same lines as in Sec. 4.4.2. By doing so, the objective is not to reproduce a similar analysis as with the steady cases, but more to investigate the evolution of the different terms for the instantaneous flow and the mean flow as compared to the laminar cases (a) and (b).

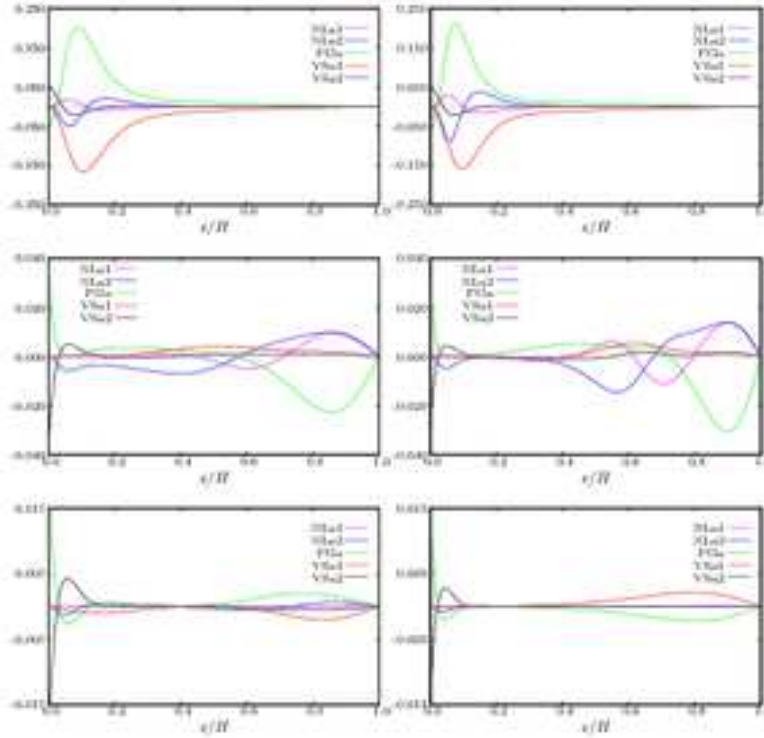


Fig. 9. Momentum balance in axial direction plotted along vertical lines at three different radial positions. First row: $r/R = 0.98$; second row: $r/R = 0.48$; third row: $r/R = 0.08$. Left column: case $Re = 900$; Right column: case $Re = 1500$. Case $\Lambda = 1$. The terminology refers to Tab. 5.

We compare the radial terms for the instantaneous and mean flows presented in Fig. 10, to their laminar and steady counterparts in Fig. 7. In terms of magnitude, the leading terms have a slightly higher magnitude at $Re = 6000$. The general observations given in Sec. 4.4.2 remain valid here for $z/H = 0.64, 0.95, 1$. However, the influence of the intense recirculation bubble modifies locally and significantly the terms in the region $0.2 \leq r/R \leq 0.4$, for the instantaneous flow. Indeed, in this interval around the radial position $r/R = 0.3$ and close to the free surface, the centrifugal acceleration $NLr2$ presents a local minimum, while the decelerating radial pressure gradient presents a local maximum. These localized effects are directly related to the presence of the recirculation bubble as can be seen in Fig. 6. A similar observation can be done for the mean flow but the effect is much less visible.

Close to the rotating disk, at $z/H = 0.03$, the variations of the five axial terms are notably different from their laminar counterparts, but extremely similar for the instantaneous and mean flows. More precisely, the viscous term VSr has mainly a dissipative action in the laminar regime, while it is slightly driving the flow at $Re = 6000$, except very close to the tubular side-wall where it gets back its dissipative action in the jet-like shear layer. Moreover, the two leading terms, namely the centrifugal acceleration $NLr2$ and the radial pressure gradient, both presents a local maximum in the region $0.2 \leq r/R \leq 0.3$, for the case (c), while it keeps growing in the laminar regime. This particular observation is again related to the presence of the recirculation bubbles in this region, which locally strongly modifies the momentum transfers. Finally, the third radial convective term $NLr3$, which is very small in the laminar regime, acquires a magnitude as important as the two other convective terms for $r/R \geq 0.9$.

Let us consider now the radial variations of the five azimuthal terms as shown in Fig. 11. A rapid

overlook of all variations for the instantaneous flow sample (left column) allows to conclude to a general agreement with the results obtained in the laminar cases (a) and (b). The variations of the different terms are similar for the instantaneous and mean flows in the outer radial region, which implies again a relative steadiness of those terms for $r/R \geq 0.7$. On the other hand, the mean flow yields vanishingly small terms in the inner core region $r/R \leq 0.4$, where the instantaneous flow have the three nonlinear convective terms $NLt1$ – $NLt3$ with a relatively high magnitude. The unsteady activity of those three nonlinear terms and the intense fluctuating activity generated by them is further discussed in Sec. 4.5.

As a last step, we compare the axial terms for the instantaneous and mean flows presented in Fig. 12 to their laminar and steady counterparts in Fig. 9. We start from the outer radial line $r/R = 0.98$, where the results for the instantaneous flow and the mean flow are extremely close, revealing an almost steady behavior of the jet-like wall shear layer surrounding the tubular side-wall. The comparison of these results with those of cases (a) and (b) leads to several comments. First, the variations of all the terms are limited to a smaller zone above the disk at $Re = 6\,000$. The magnitude of the axial pressure gradient is increased with Re . More surprisingly the axial pressure gradient is no longer counterbalanced by the convective term $NLa1$, but is now counterbalanced by $NLa2$. By extension, one can infer that the jet-like shear layer is dominated by axial effects at high Reynolds number.

For the two other radii $r/R = 0.08, 0.48$, the instantaneous flow terms are far different from their mean counterparts. As consequence, the flow in the inner core region appears much more unsteady than the flow in the outer region of the cavity. In addition, given the high level of fluctuation in the inner core region of the flow—see Fig. 17—it appears irrelevant to further analyze the results for the mean flow. On the other hand, variations of the different axial terms for the instantaneous flow reveals that the axial momentum transfers are more important at high Re and are predominant in the top half of the cavity, including below the free surface. Also, not shown here, the viscous terms are still insignificant and the two axial convective terms $NLa1$ and $NLa2$, and the axial pressure gradient dominate the transfers with other unsteady and nonaxisymmetric terms.

4.5 *Nonaxisymmetric modes in the unsteady transitional flow*

All the previous results dealing with the transitional case (c) reveals a complex flow dynamics due to instabilities developing from a steady stable flow similar to the steady laminar cases (a) and (b). The objective of this section is to discuss the physical origin of this instability based on the results presented earlier and also to characterize, at least qualitatively, its effect on the flow field.

As mentioned on several occasions in Sec. 4.3 and Sec. 4.4, the inner core region of the flow $r/R \leq 0.2$ is globally governed by a quasi-solid-body rotation and in the outer radial region, a wall-jet along the tubular side-wall drives the flow. As already discussed, this latter axial wall-jet is turned into a radial surface jet by the presence of the free surface. It seems therefore legitimate to consider the interfacial zone—denoted Υ in the sequel—between the inner core region and the radially-inward coming jet as prone to developing instabilities. Given the stress-free condition imposed on the free surface, the effect of the instabilities should persist all the way to the free

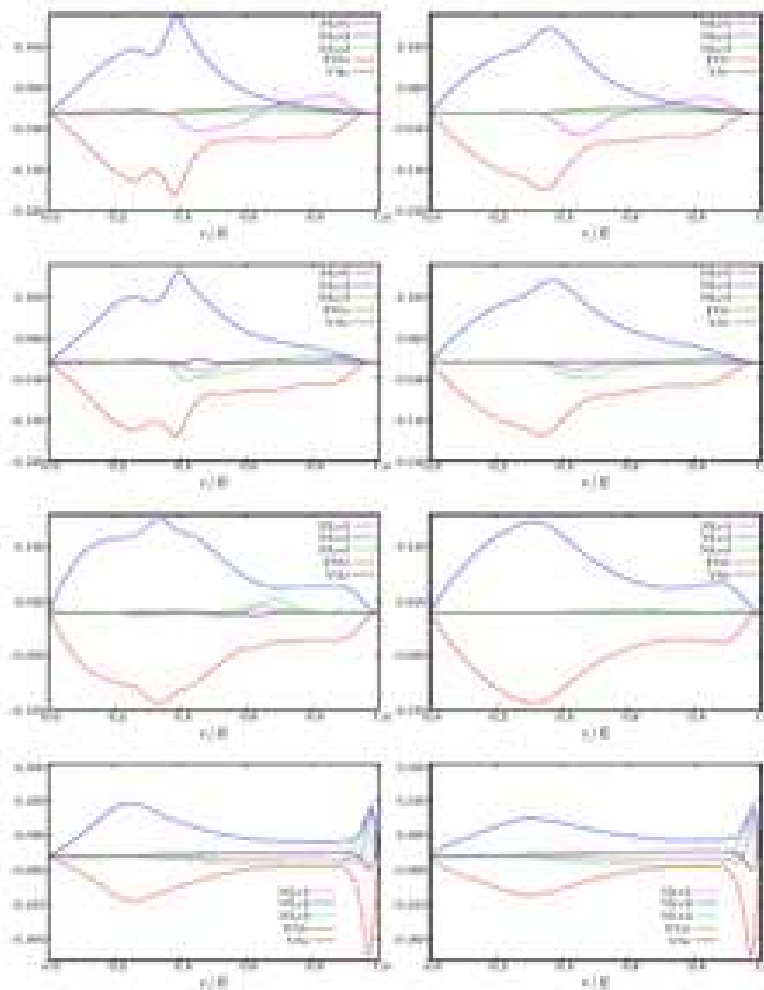


Fig. 10. Momentum balance in radial direction plotted along horizontal radial lines at four different vertical positions. First row: $z/H = 1$; second row: $z/H = 0.95$; third row: $z/H = 0.64$; fourth row: $z/H = 0.03$. Left column: instantaneous flow; Right column: mean flow. Case $\Lambda = 1$ and $\text{Re} = 6000$. The terminology refers to Tab. 5.

surface itself. Consequently, we consider the variations at the free surface $z/H = 1$ of the radial and azimuthal velocity components—the axial component vanishes at the free surface because of the kinematic boundary condition on it—and of the axial angular momentum $\Gamma = ru_\theta$. These variations for the instantaneous flow are shown in Fig. 18 (top row), while the corresponding rms fluctuations are presented in the row below.

The most significant feature highlighted in these graphs is the presence of an annular region with $0.3 \leq r/R \leq 0.4$, where the fluctuations of u_r , u_θ and Γ are intense. Such intense fluctuating activity brings the interfacial zone Υ to light. Focusing now on the rms fluctuations of the axial angular momentum, one may notice the presence of a second outer annular region comprised in the interval $0.6 \leq r/R \leq 0.9$, which is nonaxisymmetric and relatively intense. This outer region of intense rms fluctuations for Γ correspond to the zone where the jet-like shear layer is turned into the interior by the free surface. This outer wall jet injects high-angular-momentum fluid towards the cylinder axis. This radial jet impinges on the cylindrical core of the fluid that is in solid-body rotation. When increasing the Reynolds number, the radius of the cylindrical core in solid-body rotation is reduced, while the intensity of the radial jet is increased. Above a given

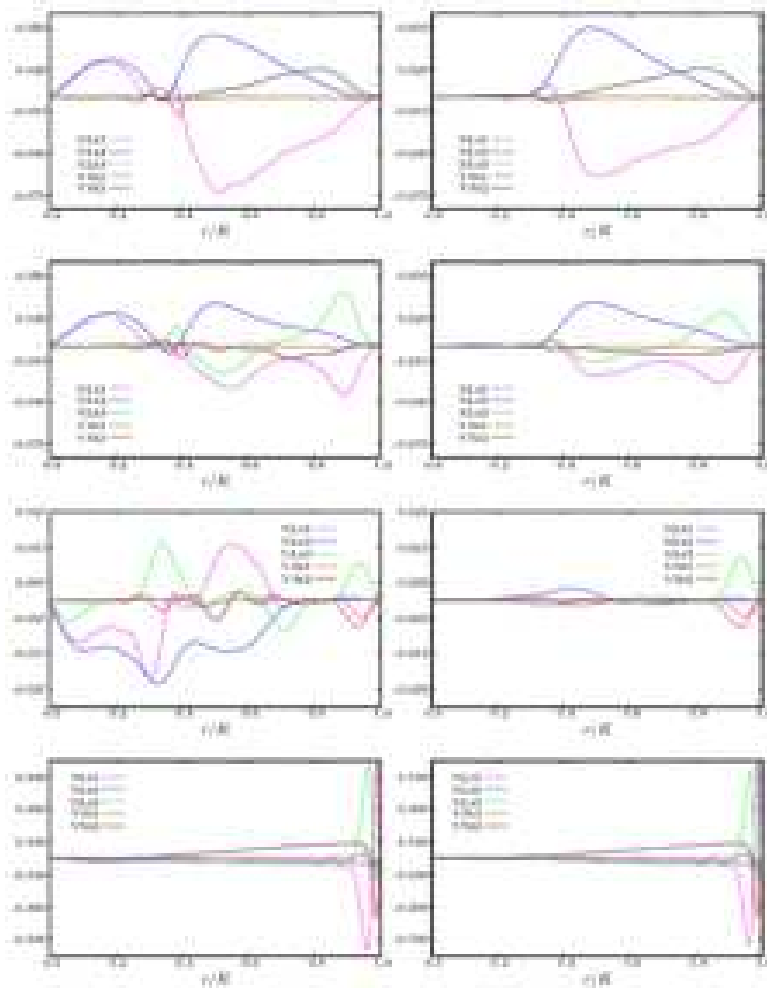


Fig. 11. Momentum balance in azimuthal direction plotted along horizontal radial lines at four different vertical positions. First row: $z/H = 1$; second row: $z/H = 0.95$; third row: $z/H = 0.64$; fourth row: $z/H = 0.03$. Left column: instantaneous flow; Right column: mean flow. Case $\Lambda = 1$ and $Re = 6000$. The terminology refers to Tab. 5.

value of the Reynolds number, the action of the impingement of the radial jet on the inner core region starts developing unstable modes.

The origin of these unstable modes is to be found in the analysis of the momentum transfers performed in the previous section. Returning on the radial variations of the five azimuthal terms below the free surface at $z/H = 0.95$, Fig. 13 reproduces these variations for $Re = 900, 1500, 6000$ (instantaneous flow), 6000 (mean flow) from top to bottom. All these results have been shown separately before and are now shown together to facilitate the discussion. The flow in the outer region $r/R > 0.5$ has a strong steady character given the fact that the variations for the mean flow are fairly close to those of the instantaneous flow. The Coriolis term $NLt2 = -u_r u_\theta / r$ keeps the same radially-outward decreasing trend. On the other hand, the two other nonlinear terms $NLt1$ and $NLt3$ develop opposed and equally-intense peaks around $r/R = 0.9$. These opposite peaks have an increasing intensity with the Reynolds number. In the interfacial zone Υ , all the terms involved present brutal variations and changes of behavior, which give another characterization of this interfacial zone Υ . In the inner core region $r/R \leq 0.4$, the flow possesses a strong unsteady character brought to light by the vanishingly small values of the

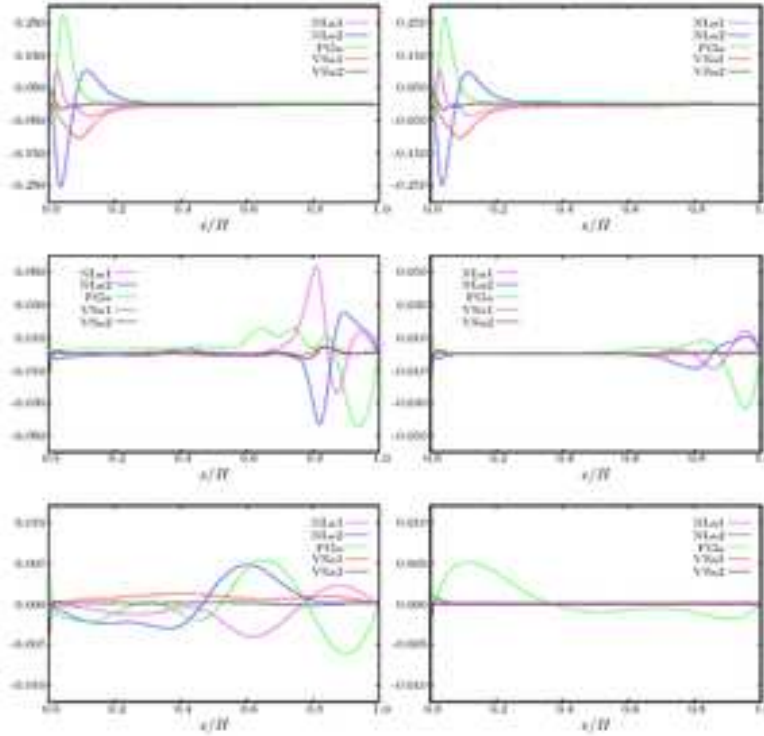


Fig. 12. Momentum balance in axial direction plotted along vertical lines at three different radial positions. First row: $r/R = 0.98$; second row: $r/R = 0.48$; third row: $r/R = 0.08$. Left column: instantaneous flow; Right column: mean flow. Case $\Lambda = 1$ and $Re = 6000$. The terminology refers to Tab. 5.

various terms for the mean flow. Consequently, the unstable azimuthal modes are to be found into this inner cylindrical region. Indeed, one may notice that the convective term $NLt1 = -u_r \partial u_\theta / \partial r$ and the Coriolis term $NLt2 = -u_r u_\theta / r$ are negative and have a low magnitude in the laminar cases (a) and (b), but acquires large positive values at $Re = 6000$. Moreover, all the three other terms $NLt3$, $VSt1$ and $VSt2$ have very low magnitudes, and thus cannot counterbalance the azimuthal momentum injected by $NLt1$ and the Coriolis term $NLt2$. Only an unsteady and nonaxisymmetric flow can support such azimuthal momentum effects. The effect of these two destabilizing terms on the flow apparently leads to the formation of azimuthal rotating waves superimposed to the stable base flow. The variations at the free surface $z/H = 1$, of the radial and azimuthal velocity components, and of the axial angular momentum shown in Fig. 18 (top row), suggest the conjugate effect of several rotating waves. These rotating waves correspond to even azimuthal Fourier modes, mainly $n = 2$ and $n = 4$.

5 Conclusions

The incompressible flow of a viscous fluid enclosed in a cylindrical container with an open top flat surface and driven by the constant rotation of the bottom wall has been thoroughly investigated. The top surface of the cylindrical cavity is left open with a stress-free boundary condition imposed on it. No-slip condition is imposed on the side-wall and also on the rotating bottom end-wall by means of a regularized angular velocity profile. More specifically, the stress-free top surface is maintained fixed and flat.

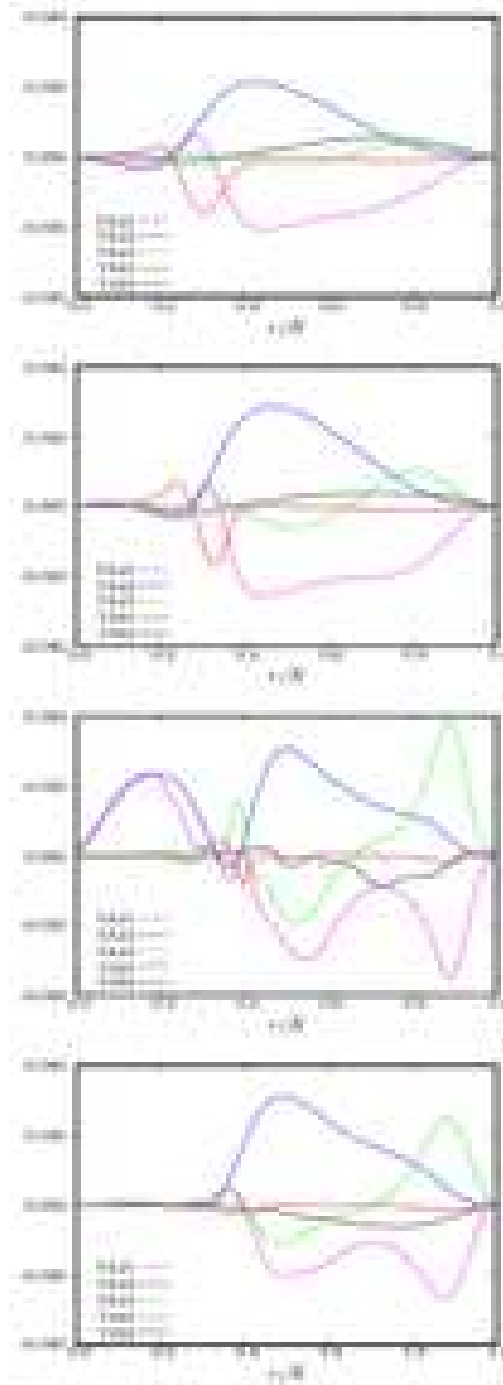


Fig. 13. Momentum terms in azimuthal direction plotted along the horizontal radial line at $z/H = 0.95$. From top to bottom: case (a); case (b); case (c) instantaneous; case (c) mean flow. The terminology refers to Tab. 5.

New flow states have been investigated based on a fully three-dimensional solution of the Navier–Stokes equations for the free-surface cylindrical swirling flow, without resorting to any symmetry property unlike all other results available in the literature. To our knowledge, the present study delivers the most general available results for this flat-free-surface problem due to its original mathematical treatment.

Five different cases corresponding to different pairs of governing parameters (Λ, Re) have been

considered. The Reynolds regime corresponds to transitional flows with some incursions in the fully laminar regime. Both steady and unsteady non-oscillatory swirling flows are considered with a particular emphasis on the case ($\Lambda = 1$, $Re = 6\,000$). Of great concern to this study is the question of space resolution. This is particularly important for the bifurcated case at $Re = 6\,000$. Convergence tests in space and time have been carried out on this upmost problematic case, and optimal values of the polynomial degree and time-step have been deduced.

The evolution of the total kinetic energy of this open flow has been carefully studied for increasing Reynolds numbers and has been compared to the results for the closed swirling flow. The presence of the free surface on the top of the cylinder is found to strongly modify the observed trend: the total kinetic energy is increased with Re in the open cylinder case, while the converse is observed in the closed cylinder case. A physical analysis of the energetic action of the surface layer below the free surface allows to justify the above results. A comprehensive physical description of all flow states has been given with particular emphasis on the vortex breakdown bubbles and on the structure of the vortex lines. The unsteady case at $Re = 6\,000$ has retained more attention, given its unsteady transitional character. The mean flow and the corresponding rms fluctuations have been calculated and the results analyzed accordingly. The momentum transfers in the radial, azimuthal and axial directions have been studied along various one-dimensional lines. For the transitional case at $Re = 6\,000$, the flow in an inner cylindrical core is in solid-body rotation, while the outer radial layer is dominated by the jet-like shear layer along the tubular side-wall. This axial wall-jet is turned into a radial jet of angular momentum, which prevails all the way up to the free surface. The impingement of this radial jet onto the inner cylindrical core in solid-body rotation leads to the development of unstable azimuthal modes. The nonlinear terms, which includes a Coriolis effect, responsible for the development of these unstable modes have been found using the azimuthal momentum imbalance below the free surface. These unstable modes take the form of even-order azimuthal rotating waves.

Acknowledgements

This research is being partially funded by a Swiss National Science Foundation Grant (No. 200020-101707) whose supports are gratefully acknowledged.

The results were obtained on supercomputing facilities on the Pleiades clusters at EPFL-IGM.

References

- [1] P. N. Shankar, M. D. Deshpande, Fluid Mechanics in the Driven Cavity, *Annu. Rev. Fluid Mech.* 32 (2000) 93–136.
- [2] V. Y. A. Bogatyrev, A. V. Gorin, End effects in rectangular cavities, *Fluid. Mech.-Soviet Res.* 7 (1978) 101–106.
- [3] J. R. Koseff, R. L. Street, The lid-driven cavity flow: A synthesis of qualitative and quantitative observations, *J. Fluids Eng.-Transactions ASME* 106 (1984) 390–398.

- [4] J. R. Koseff, R. L. Street, Visualization studies of a shear driven 3-dimensional recirculating flow, *J. Fluids Eng.-Transactions ASME* 106 (1984) 21–29.
- [5] H. M. Blackburn, J. M. Lopez, Symmetry breaking of the flow in a cylinder driven by a rotating end wall, *Phys. Fluids* 12 (2000) 2698–2701.
- [6] H. M. Blackburn, J. M. Lopez, Modulated rotating waves in an enclosed swirling flow, *J. Fluid Mech.* 465 (2002) 33–58.
- [7] J. N. Sørensen, Visualization of rotating fluid flow in a closed cylinder, Tech. rep., Department of Fluid Mechanics, Technical University of Denmark, rep. AFM 92–06 (1992).
- [8] A. Spohn, M. Mory, E. J. Hopfinger, Experiments on vortex breakdown in a confined flow generated by a rotating disc, *J. Fluid Mech.* 370 (1998) 73–99.
- [9] F. Sotiropoulos, Y. Ventikos, Transition from bubble-type vortex breakdown to columnar vortex in a confined swirling flow, *Int. J. Heat Fluid Flow* 19 (1998) 446–458.
- [10] J. C. F. Pereira, J. M. M. Sousa, Confined vortex breakdown generated by a rotating cone, *J. Fluid Mech.* 385 (1999) 287–323.
- [11] F. Sotiropoulos, Y. Ventikos, The three-dimensional structure of confined swirling flows with vortex breakdown, *J. Fluid Mech.* 426 (2001) 155–175.
- [12] H. U. Vogel, Experimentelle Ergebnisse über die laminare Strömung in einem zylindrischen Gehäuse mit darin rotierender scheinbe, Tech. rep., Max-Planck-Institut für Strömungsforschung, Göttingen, bericht 6 (1968).
- [13] R. Ronnenberg, Ein selbstjustierendes 3-Komponenten-Laserdoppleranemometer nach dem Verzeichsstrahlverfahren, angewandt auf Untersuchungen in einer stationären zylinder-symmetrischen Drehströmung mit einem Rückströmgebiet, Tech. rep., Max-Planck-Institut für Strömungsforschung, Göttingen, bericht 19. (1977).
- [14] M. G. Hall, Vortex breakdown, *Annu. Rev. Fluid Mech.* 4 (1972) 195–218.
- [15] S. Leibovich, Structure of vortex breakdown, *Annu. Rev. Fluid Mech.* 10 (1978) 221–246.
- [16] V. Shtern, F. Hussain, Collapse, symmetry breaking, and hysteresis in swirling flows, *Annu. Rev. Fluid Mech.* 31 (1999) 537–566.
- [17] R. R. Kerswell, Elliptical instability, *Annu. Rev. Fluid Mech.* 34 (2002) 83–113.
- [18] R. E. A. Arndt, Cavitation in vortical flows, *Annu. Rev. Fluid Mech.* 34 (2002) 143–175.
- [19] J. H. Faler, S. Leibovich, Disrupted states of vortex flow and vortex breakdown, *Phys. Fluids* 20 (1977) 1385–1400.
- [20] M. P. Escudier, Observations of the flow produced in a cylindrical container by a rotating endwall, *Experiments In Fluids* 2 (1984) 189–196.
- [21] M. P. Escudier, J. J. Keller, Recirculation in swirling flow – a manifestation of vortex breakdown, *AIAA J.* 23 (1985) 111–116.
- [22] A. Spohn, M. Mory, E. J. Hopfinger, Observations of vortex breakdown in an open cylindrical container with a rotating bottom, *Experiments In Fluids* 14 (1993) 70–77.
- [23] K. Hourigan, L. J. W. Graham, M. C. Thompson, Spiral streaklines in pre-vortex breakdown regions of axisymmetrical swirling flows, *Phys. Fluids* 7 (1995) 3126–3128.

- [24] M. Brøns, M. C. Thompson, K. Hourigan, Dye visualization near a three-dimensional stagnation point: Application to the vortex breakdown bubble, *J. Fluid Mech.* In Press.
- [25] H. P. Pao, A numerical computation of a confined rotating flow, *J. Appl. Mech.* 37 (1970) 480–487.
- [26] H. J. Lugt, W. Haussling, Development of flow circulation in a rotating tank, *Acta Mechanica* 18 (1973) 255–272.
- [27] H. J. Lugt, H. J. Haussling, Axisymmetric vortex breakdown in rotating fluid within a container, *J. Appl. Mechanics-Transactions Asme* 49 (1982) 921–923.
- [28] D. Dijkstra, G. J. F. van Heijst, The flow between two finite rotating-disks enclosed by a cylinder, *J. Fluid Mech.* 128 (1983) 123–154.
- [29] H. J. Lugt, M. Abboud, Axisymmetrical vortex breakdown with and without temperature effects in a container with a rotating lid, *J. Fluid Mech.* 179 (1987) 179–200.
- [30] G. P. Neitzel, Streak-line motion during steady and unsteady axisymmetric vortex breakdown, *Phys. Fluids* 31 (1988) 958–960.
- [31] O. Daube, J. N. Sørensen, Numerical-simulation of the axisymmetric periodic-flow in a cylindrical tank, *Comptes Rendus De l’Académie des Sciences Série II* 308 (1989) 463–469.
- [32] J. M. Lopez, Axisymmetrical vortex breakdown. Part 1. Confined swirling flow, *J. Fluid Mech.* 221 (1990) 533–552.
- [33] G. L. Brown, J. M. Lopez, Axisymmetrical vortex breakdown. Part 2. Physical mechanisms, *J. Fluid Mech.* 221 (1990) 553–576.
- [34] J. M. Lopez, A. D. Perry, Axisymmetrical vortex breakdown. Part 3. Onset of periodic-flow and chaotic advection, *J. Fluid Mech.* 234 (1992) 449–471.
- [35] J. N. Sørensen, E. A. Christensen, Direct numerical-simulation of rotating fluid-flow in a closed cylinder, *Phys. Fluids* 7 (1995) 764–778.
- [36] J. P. Watson, G. P. Neitzel, Numerical evaluation of a vortex-breakdown criterion, *Phys. Fluids* 8 (1996) 3063–3071.
- [37] A. Y. Gelfgat, P. Z. Bar-Yoseph, A. Solan, Steady states and oscillatory instability of swirling flow in a cylinder with rotating top and bottom, *Phys. Fluids* 8 (1996) 2614–2625.
- [38] A. Y. Gelfgat, P. Z. Bar-Yoseph, A. Solan, Stability of confined swirling flow with and without vortex breakdown, *J. Fluid Mech.* 311 (1996) 1–36.
- [39] N. Tsitverblit, E. Kit, On the onset of unsteadiness in confined vortex flows, *Fluid Dyn. Res.* 23 (1998) 125–152.
- [40] M. Brøns, L. K. Voigt, J. N. Sørensen, Streamline topology of steady axisymmetric vortex breakdown in a cylinder with co- and counter-rotating end-covers, *J. Fluid Mech.* 401 (1999) 275–292.
- [41] H. M. Blackburn, J. M. Lopez, The onset of three-dimensional standing and modulated travelling waves in a periodically driven cavity flow, *J. Fluid Mech.* 497 (2003) 289–317.
- [42] A. V. Bisgaard, M. Brøns, J. N. Sørensen, Vortex breakdown generated by off-axis bifurcation in a cylinder with rotating covers, *Acta Mechanica* 187 (2006) 75–83.

- [43] W. Z. Shen, J. N. Sørensen, J. A. Michelsen, Numerical study of swirling flow in a cylinder with rotating top and bottom, *Phys. Fluids* 18 (2006) Art. 064102.
- [44] A. Y. Gelfgat, P. Z. Bar-Yoseph, A. Solan, Three-dimensional instability of axisymmetric flow in a rotating lid-cylinder enclosure, *J. Fluid Mech.* 438 (2001) 363–377.
- [45] F. Sotiropoulos, Y. Ventikos, T. C. Lackey, Chaotic advection in three-dimensional stationary vortex-breakdown bubbles: Sil’nikov’s chaos and the devil’s staircase, *J. Fluid Mech.* 444 (2001) 257–297.
- [46] F. Marques, J. M. Lopez, Precessing vortex breakdown mode in an enclosed cylinder flow, *Phys. Fluids* 13 (2001) 1679–1682.
- [47] E. Serre, P. Bontoux, Vortex breakdown in a three-dimensional swirling flow, *J. Fluid Mech.* 459 (2002) 347–370.
- [48] H. M. Blackburn, Three-dimensional instability and state selection in an oscillatory axisymmetric swirling flow, *Phys. Fluids* 14 (2002) 3983–3996.
- [49] J. M. Lopez, Rotating and modulated rotating waves in transitions of an enclosed swirling flow, *J. Fluid Mech.* 553 (2006) 323–346.
- [50] M. Piva, E. Meiburg, Steady axisymmetric flow in an open cylindrical container with a partially rotating bottom wall, *Phys. Fluids* 17 (2005) Art. 063603.
- [51] V. L. Okulov, J. N. Sørensen, L. K. Voigt, Vortex scenario and bubble generation in a cylindrical cavity with rotating top and bottom, *European J. Mechanics B-Fluids* 24 (2005) 137–148.
- [52] T. Mullin, J. J. Kobine, S. J. Tavener, K. A. Cliffe, On the creation of stagnation points near straight and sloped walls, *Phys. Fluids* 12 (2000) 425–431.
- [53] M. Brøns, L. K. Voigt, J. N. Sørensen, Topology of vortex breakdown bubbles in a cylinder with a rotating bottom and a free surface, *J. Fluid Mech.* 428 (2001) 133–148.
- [54] L. Mununga, K. Hourigan, M. C. Thompson, T. Leweke, Confined flow vortex breakdown control using a small rotating disk, *Phys. Fluids* 16 (2004) 4750–4753.
- [55] D. Lo Jacono, J. N. Sørensen, M. C. Thompson, K. Hourigan, Control of vortex breakdown in a closed cylinder with a small rotating rod, *J. Fluids Struct.* In Press.
- [56] D. T. Valentine, C. C. Jahnke, Flows induced in a cylinder with both end walls rotating, *Phys. Fluids* 6 (1994) 2702–2710.
- [57] J. M. Lopez, Unsteady swirling flow in an enclosed cylinder with reflectional symmetry, *Phys. Fluids* 7 (1995) 2700–2714.
- [58] R. Iwatsu, Numerical study of flows in a cylindrical container with rotating bottom and top flat free surface, *J. Phys. Soc. Japan* 74 (2005) 333–344.
- [59] R. Iwatsu, Analysis of flows in a cylindrical container with rotating bottom and top undeformable free surface, *JSME Int. J. Series B-Fluids Thermal Engineering* 47 (2004) 549–556.
- [60] J. M. Lopez, F. Marques, A. H. Hirs, R. Miraghaie, Symmetry breaking in free-surface cylinder flows, *J. Fluid Mech.* 502 (2004) 99–126.
- [61] R. Bouffanais, M. O. Deville, E. Leriche, Large-eddy simulation of the flow in a lid-driven cubical cavity, *Phys. Fluids* 19 (2007) Art. 055108.

- [62] T. Sarpkaya, Vorticity, free surface, and surfactants, *Annu. Rev. Fluid Mech.* 28 (1996) 83–128.
- [63] M. O. Deville, P. F. Fischer, E. H. Mund, *High-order methods for incompressible fluid flow*, Cambridge University Press, Cambridge, 2002.
- [64] Y. Maday, A. T. Patera, *Spectral element methods for the incompressible Navier–Stokes equations*, *State-of-the-Art Survey on Computational Mechanics*, A. K. Noor & J. T. Oden Eds., ASME, New-York, 1989, pp. 71–142.
- [65] Y. Maday, D. Meiron, A. T. Patera, E. M. Rønquist, Analysis of iterative methods for the steady and unsteady Stokes problem - Application to spectral element discretizations, *SIAM J. Sci. Comput.* 14 (1993) 310–337.
- [66] N. Bodard, R. Bouffanais, M. O. Deville, Solution of moving boundary problems by the spectral element method, *App. Num. Math.* 58 (2007) 968–984.
- [67] M. A. Habisreutinger, R. Bouffanais, E. Leriche, M. O. Deville, A coupled approximate deconvolution and dynamic mixed scale model for large-eddy simulation, *J. Comput. Phys.* 224 (2007) 241–266.
- [68] G. E. Karniadakis, M. Israeli, S. A. Orszag, High-order splitting methods for the incompressible Navier–Stokes equations, *J. Comput. Phys.* 97 (1991) 414–443.
- [69] R. Bouffanais, *Simulation of shear-driven flows: transition with a free surface and confined turbulence*, Ph.D. thesis, no. 3837, École Polytechnique Fédérale de Lausanne (2007).
- [70] P. J. Zandbergen, D. Dijkstra, von Kármán swirling flows, *Annu. Rev. Fluid Mech.* 19 (1987) 465–491.
- [71] L. Shen, X. Zhang, D. K. P. Yue, G. S. Triantafyllou, The surface layer for free-surface turbulent flows, *J. Fluid Mech.* 386 (1999) 167–212.
- [72] L. Shen, G. S. Triantafyllou, D. K. P. Yue, Turbulent diffusion near a free surface, *J. Fluid Mech.* 407 (2000) 145–166.
- [73] D. L. Young, H. J. Sheen, T. Y. Hwu, Period-doubling route to chaos for a swirling flow in an open cylindrical container with a rotating-disk, *Experiments In Fluids* 18 (1995) 389–392.
- [74] R. Miraghaie, J. M. Lopez, A. H. Hirs, Flow induced patterning at the air-water interface, *Phys. Fluids* 15 (2003) L45–L48.
- [75] J. M. Lopez, F. Marques, Mode competition between rotating waves in a swirling flow with reflection symmetry, *J. Fluid Mech.* 507 (2004) 265–288.
- [76] E. Leriche, S. Gavrilakis, Direct numerical simulation of the flow in the lid-driven cubical cavity, *Phys. Fluids* 12 (2000) 1363–1376.
- [77] S. L. Bragg, W. R. Hawthorne, Some exact solutions of the flow through annular cascade actuator discs, *J. Aeronaut. Sci* 17 (1950) 243.
- [78] J. J. Keller, A pair of stream functions for three-dimensional vortex flows, *Zeitschrift für Angewandte Mathematik und Physik* 47 (1996) 821–836.

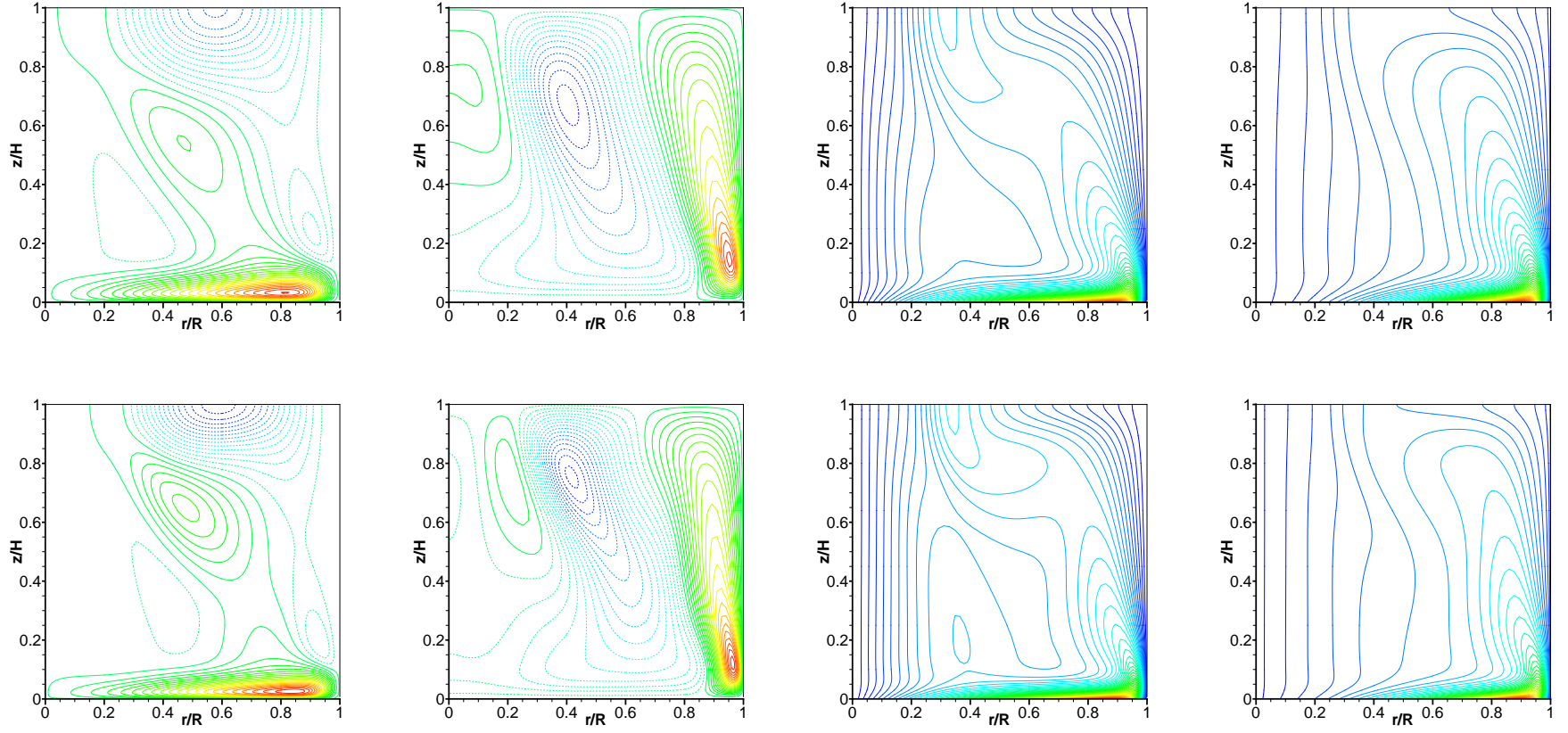


Fig. 14. Contours in a meridional plane for the case $\Lambda = 1$. Top row: case $\text{Re} = 900$; Bottom row: case $\text{Re} = 1500$. From left column to right column: radial velocity component u_r ; axial velocity component $w = u_z$; azimuthal velocity component u_θ ; axial angular momentum component $\Gamma = ru_\theta$. The 35 contours are uniformly spaced, between -0.1 and 0.145 for u_r ; and between -0.08 and 0.115 for u_z ; The 50 contours are uniformly spaced, between 0 and 1 for u_θ and Γ .

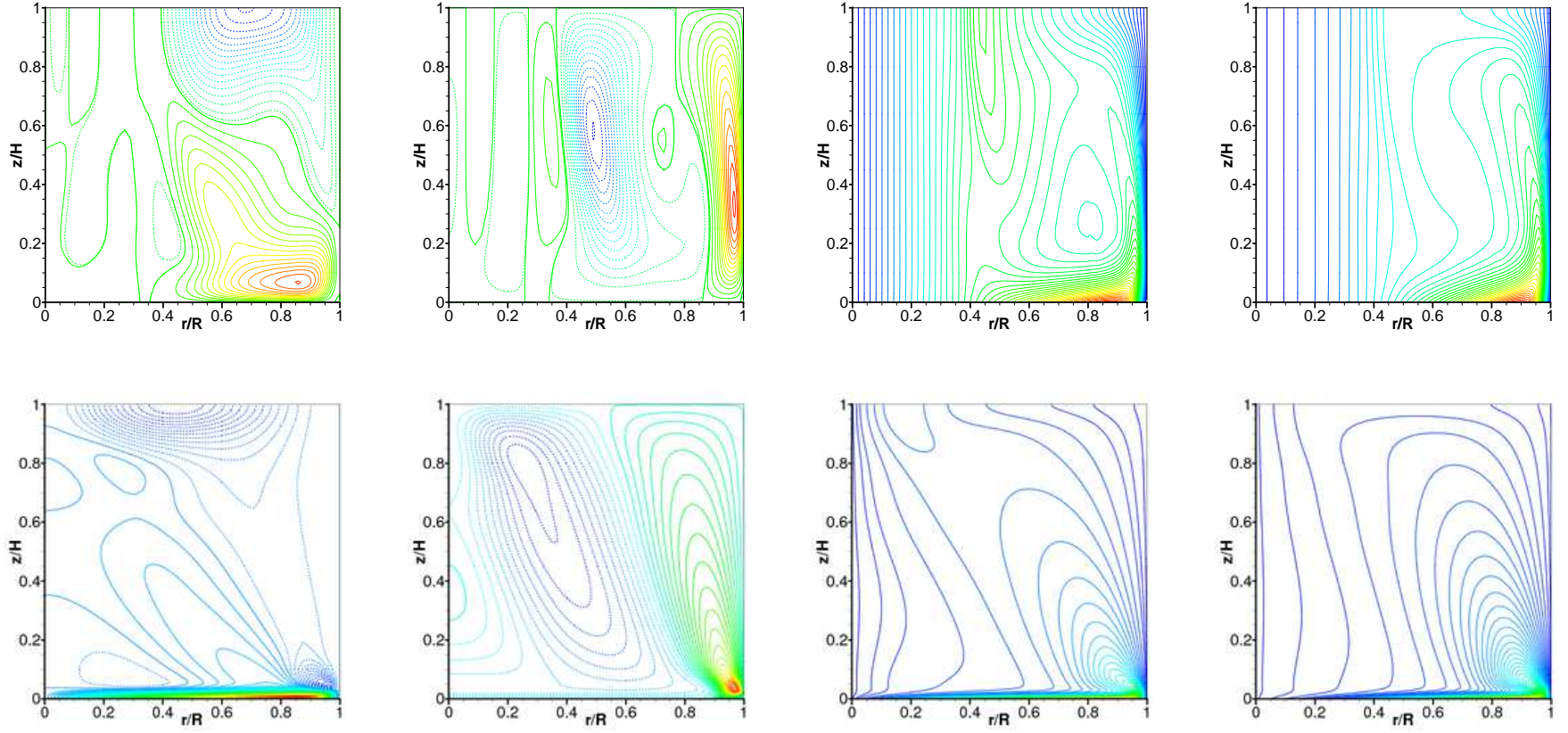


Fig. 15. Contours in a meridional plane for the case (d) : $(\Lambda = 1/3, \text{Re} = 2000)$ (top row) and case (e) : $(\Lambda = 3, \text{Re} = 2000)$ (bottom row). From left column to right column: radial velocity component u_r ; axial velocity component $w = u_z$; azimuthal velocity component u_θ ; axial angular momentum component $\Gamma = ru_\theta$. All contours are uniformly spaced; 35 contours between -0.17 and 0.15 for u_r case (d) ; 90 contours between -0.03 and 0.15 for u_r case (e) ; 35 contours between -0.1 and 0.12 for u_z case (d) ; 35 contours between -0.05 and 0.12 for u_z case (e) ; 50 contours between 0 and 1 for u_θ and Γ , cases (d) and (e) .

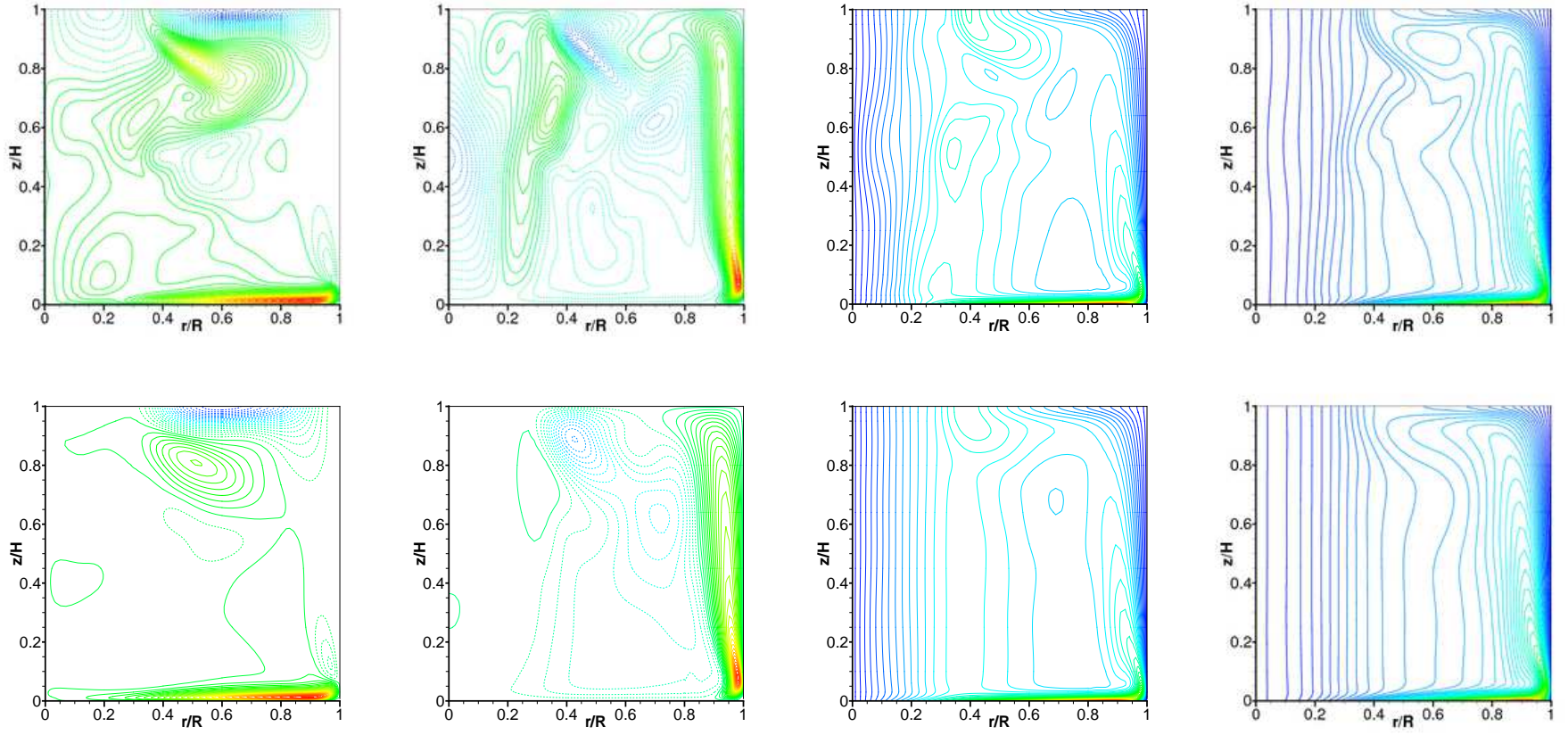


Fig. 16. Contours in a meridional plane for the case $\Lambda = 1$ and $\text{Re} = 6000$. Top row: instantaneous flow; Bottom row: mean flow. From left column to right column: radial velocity component u_r ; axial velocity component u_z ; azimuthal velocity component u_θ ; axial angular momentum $\Gamma = ru_\theta$. The 50 contours are uniformly spaced, between -0.13 and 0.16 for u_r ; between -0.09 and 0.14 for u_z ; and between 0 and 1 for u_θ . The 100 contours are uniformly spaced between 0 and 1 for Γ .

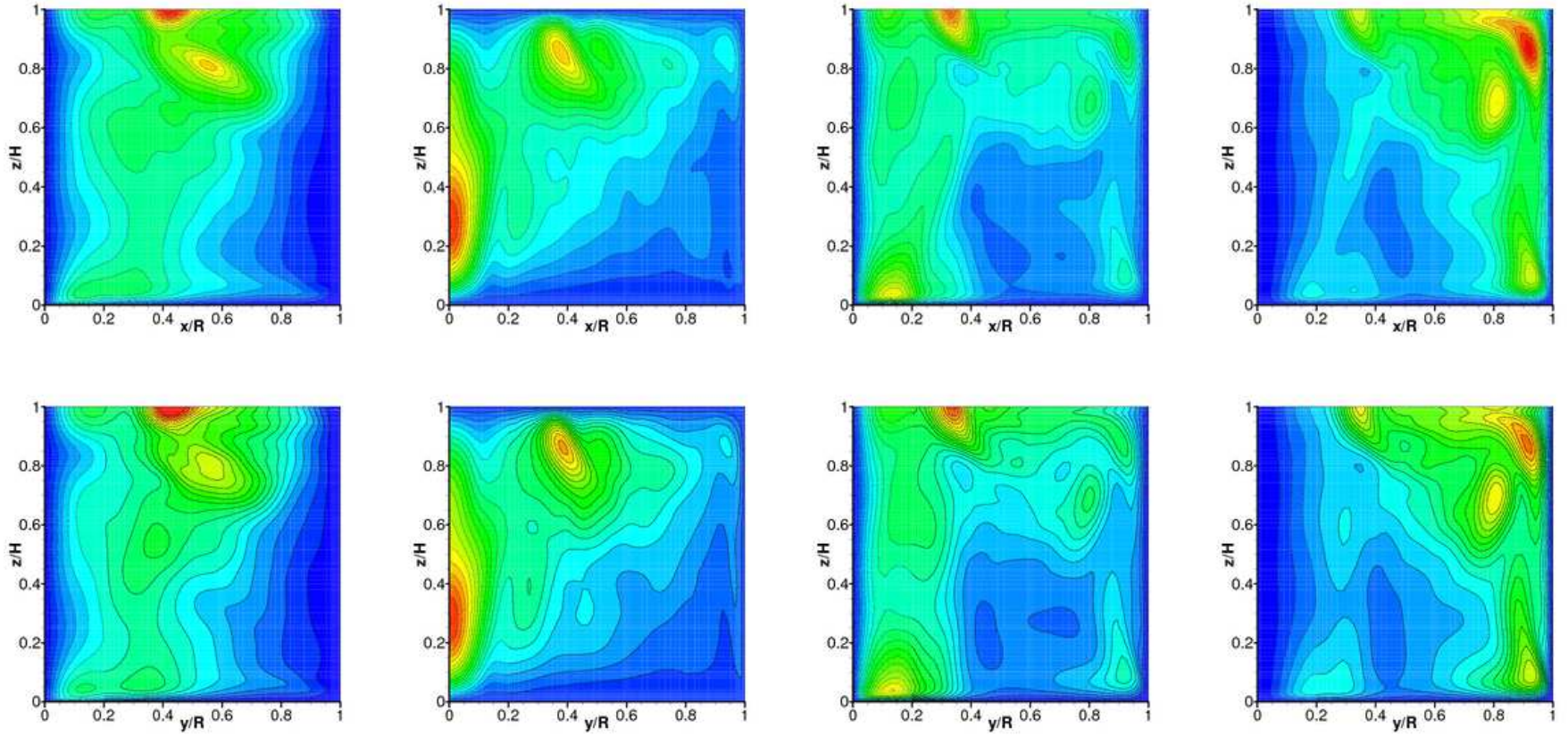


Fig. 17. Contours in a meridional plane for the case $\Lambda = 1$ and $\text{Re} = 6000$. Top row: in the meridional plane $y/R = 0$; Bottom row: in the meridional plane $x/R = 0$. From left column to right column: rms fluctuations of radial velocity component u_r ; rms fluctuations of the axial velocity component u_z ; rms fluctuations of the azimuthal velocity component u_θ ; and rms fluctuations of the axial angular momentum $\Gamma = ru_\theta$. The 20 contours are uniformly spaced, between 0 and 0.002 for rms- u_r ; between 0 and 0.0024 for rms- u_z ; between 0 and 0.004 for rms- u_θ ; and between 0 and 0.001 for rms- Γ .

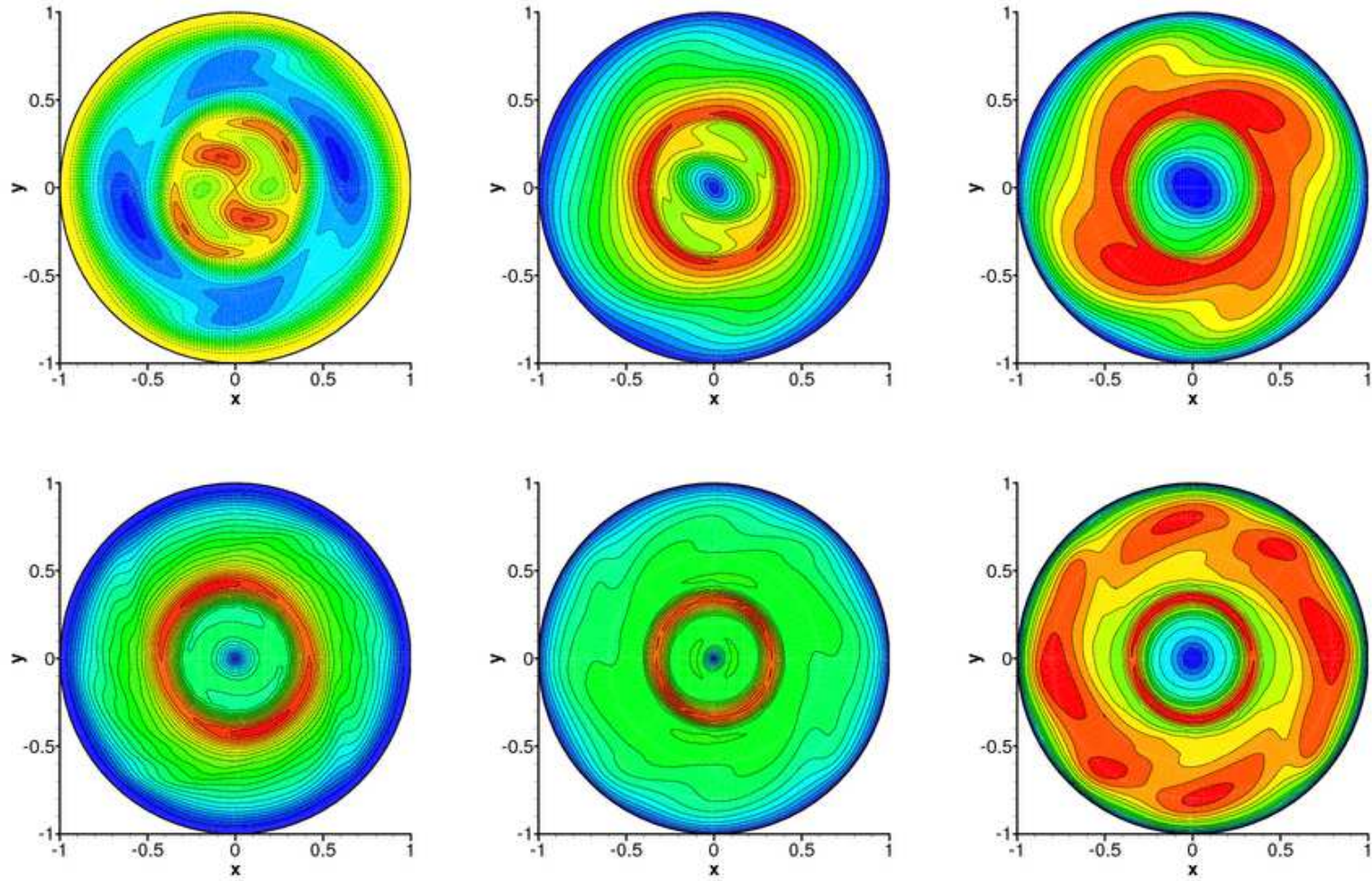


Fig. 18. Contours on the free surface $z/H = 1$ for the case $\Lambda = 1$ and $Re = 6000$. Top row: instantaneous flow; Bottom row: rms fluctuations. Left column: radial velocity component u_r ; Central column: azimuthal velocity component u_θ ; Right column: axial component of the angular momentum $\Gamma = ru_\theta$. The 15 contours are uniformly spaced, between -0.13 and 0.03 for u_r ; between 0 and 0.35 for u_θ ; and between 0 and 0.2 for Γ . The 20 contours are uniformly spaced, between 0 and 0.002 for $\text{rms-}u_r$; between 0 and 0.024 for $\text{rms-}u_\theta$; and between 0 and 0.001 for $\text{rms-}\Gamma$.

